Fall 2018

Developing improved techniques for GPR guided wave data analysis

Yunyi Guan

Department:

DEVELOPING IMPROVED TECHNIQUES FOR GPR GUIDED WAVE DATA ANALYSIS

by

YUNYI GUAN

A THESIS

Presented to the Faculty of the Graduate School of the

MISSOURI UNIVERSITY OF SCIENCE AND TECHNOLOGY

In Partial Fulfillment of the Requirements for the Degree

MASTER OF SCIENCE IN GEOLOGICAL ENGINEERING

2018

Approved by:

Katherine Grote, Advisor
Neil L. Anderson
J. David Rogers

ABSTRACT

This study was conducted to investigate how limiting the allowable velocity range when analyzing guided wave data will affect the results of dielectric permittivity and thickness estimation. We conducted four sets of Experiments: an underlying layer of saturated organic loam is covered by incremental layers of the dry organic loam; a base layer of dry organic loam covered by the saturated organic loam; a saturated basal layer of silt with overlying dry silt layers, and a base layer of dry silt overlain by saturated silt layers to conduct a comparative study and perform three surveys for each of these three frequencies at 250 MHz, 500 MHz, and 1000 MHz It is concluded that from the aspect of water content, the location of the selected points has no effect on the final result; and from the aspect of soil structure, in most cases, for organic loam layers, the lower the starting phase velocity, the more accurate the results; for silt layers, the pattern is the opposite, the higher the starting point, the more accurate the results. For the fundamental mode, choosing the maximum starting phase velocity is usually best or equivalent to choosing a lower starting phase velocity. For some wet soils that have low attenuation, it may be better to choose a lower starting phase velocity. The error of inversion is less for lower starting phase velocities, so this should be considered when evaluating the accuracy of inversion estimates.

ACKNOWLEDGEMENTS

I would like to express my deep respect and appreciate to my advisor, Dr. Katherine Grote, for her patient and gratuitous help during the period of this research. I would also like to thank my committee members Dr. David Rogers and Dr. Neil L. Anderson for their insightful comments.

TABLE OF CONTENTS

Page

ABSTRACT iii

ACKNOWLEDGEMENTS iv

LIST OF ILLUSTRATIONS vii

LIST OF TABLES x

SECTION

1. INTRODUCTION 1

1.1. GUIDED WAVES FORMATION 1

1.2. PREVIOUS RESEARCH USING GPR DISPERSIVE WAVES 1

2. METHOD 13

2.1. DATA ACQUISITION 13

2.1.1. Soil Preparation. 14

2.1.2. Soil Placement. 14

2.1.3. GPR Data Acquisition Parameters. 15

2.1.4. Monitoring Soil Water Content. 15

2.2. DATA PROCESSING 17

2.2.1. Waveguide Model and Theoretical Dispersion Curve. 17

2.2.2.Determination of Phase Velocity Spectrum from CMP Data. 20

2.2.3. Inversion of Dispersion Curve. 22

2.2.4. Use MATLAB to Processing Data. 22

3. RESULTS 23

4. CONCLUSION 33

REFERENCES 45

VITA 47

LIST OF ILLUSTRATIONS

Figure Page

1.1. Guided waves are trapped within a thin surficial layer. 2

1.2. Leaky waveguide and low-velocity waveguide 2

1.3. The head and body waves in the 3D FDTD modeling electric field, where the yellow circle is the identified TE0 and TE1 modes. 3

1.4. The group velocity and phase velocity obtained from the collected CMP data set 5

1.5. Frequency-band analysis of data set for frequency ranges. 6

1.6. Phase velocity spectrum of TE mode data. 7

1.7. The configuration used by the researchers, which was developed by the EM leaky waveguide model. 10

1.8. The apparatus used in the concrete Experiment. 10

1.9. Radargram (a), phase velocity spectrum and selected dispersion curve (b) for TE configuration obtained at the Montemezzo test site. 11

1.10. Radargram (a), phase velocity spectrum and selected dispersion 12

1.11. Misfit function of the inverted profile of the Montemezzo site (a) and Cervinia site (b). 12

2.1. The Experimental tank was constructed with no metal and filled with horizontal layers of soil. In this figure, 250 MHz antennas are being moved over dry sand. 17

2.2. Diagram of (a) the TE and (b) TM source-receiver configurations. 18

3.1. Diagram (a) max phase velocity (user selected 0.35 m/ns as the maximum velocity, but the algorithm selected the actual starting velocity as 0.3 m/ns) for Experiment 3 at 250 MHz. (b) Result figure of max phase velocity. 27

3.2. Diagram (a) phase velocity starting at 0.2 m/ns (user selected 0.2 m/ns, but the algorithm selected the actual starting velocity as 0.21 m/ns) for Experiment 3 at 250 MHz. (b) Result figure of phase velocity starting at 0.2 m/ns 27

3.3. Diagram (a) phase velocity starting at 0.15 m/ns (choose at 0.15 m/ns which actual starting at 0.14 m/ns) for Experiment 3 at 250 MHz. (b) Result figure of phase velocity starting at 0.15 m/ns. 28

3.4. Diagram (a) max phase velocity (choose at 0.35 m/ns which actual starting at 0.35 m/ns) for starting point for Experiment 4 at 500 MHz. (b) Result figure of max phase velocity. 28

3.5. Diagram (a) phase velocity starting at 0.2 m/ns (choose at 0.2 m/ns which actual starting at 0.19 m/ns) for Experiment 4 at 500 MHz. (b) Result figure of phase velocity starting at 0.2 m/ns. 29

3.6. Diagram (a) phase velocity starting at 0.15 m/ns (choose at 0.15 m/ns which actual starting at 0.15 m/ns) for Experiment 4 at 500 MHz. (b) Result figure of phase velocity starting at 0.15 m/ns. 29

3.7. Diagram (a) max phase velocity (choose at 0.35 m/ns which actual starting at 0.35 m/ns) for starting point for Experiment 5 at 1000 MHz. (b) Result figure of max phase velocity. 30

3.8. Diagram (a) phase velocity starting at 0.2 m/ns (choose at 0.2 m/ns which actual starting at 0.225 m/ns) for Experiment 5 at 1000 MHz. (b) Result figure of phase velocity starting at 0.2 m/ns. 30

3.9. Diagram (a) phase velocity starting at 0.15 m/ns (choose at 0.15 m/ns which actual starting at 0.17 m/ns) for Experiment 5 at 1000 MHz. (b) Result figure of phase velocity starting at 0.15 m/ns. 31

3.10. Diagram (a) max phase velocity (choose at 0.35 m/ns which actual starting at 0.32 m/ns) for starting point for Experiment 3 at 1000 MHz. (b) Result figure of max phase velocity. 31

3.11. Diagram (a) phase velocity starting at 0.2 m/ns (choose at 0.2 m/ns which actual starting at 0.22 m/ns) for starting point for Experiment 3 at 1000 MHz. (b) Result figure of phase velocity starting at 0.2 m/ns. 32

4.1. Experiment 3, permittivity (all layers) where both max and 0.2 m/ns data exist 34

4.2. Experiment 3, thickness (all layers) where both max and 0.2 m/ns data exist 34

4.3. Experiment 4, 1000 MHz, permittivity and thickness error for three phase velocities 36

4.4. Experiment 4, 500 MHz, permittivity and thickness error for three phase velocities 37

4.5. Experiment 4, 250 MHz, permittivity and thickness error for three phase velocities 40

4.6. Experiment 5, permittivity (all layers) where both max and 0.2 m/ns data exist 40

4.7. Experiment 5, thickness (all layers) where both max and 0.2 m/ns data exist 40

4.8. Experiment 6, permittivity (all layers) where both max and 0.2 m/ns data exist 41

4.9. Experiment 6, thickness (all layers) where both max and 0.2 m/ns data exist 41

LIST OF TABLES

Table Page

3.1. Materials of each experiment. 24

1. INTRODUCTION

1.1. GUIDED WAVES FORMATION

When the dielectric permittivity of the overlying surface layer and the basal layer is significantly different, a reflection is caused. If the overlying surface layer is thin, the reflected energy may be trapped in the thin surface layer, which then acts as a waveguide (Figure 1.1). If the energy is thus trapped, it can form a series of interfering multiples referred to as dispersive waves. There are two types of waveguides, leaky and low-velocity. Leaky waveguides occur when the dielectric permittivity of the overlying surface layer is smaller than the dielectric permittivity of the base layer, which is when the high-velocity soil covers the low-velocity soil, and part of the energy propagates to the basal layer (Figure 1.2-a). Low-velocity waveguides occur when the dielectric permittivity of the overlying surface layer is greater than the dielectric permittivity of the basal layer, which is when the upper layer of low-velocity soil covers the base layer of high-velocity soil. In this condition, the energy will form a total reflection beyond the critical angle, and most of the energy will remain in the waveguide (Figure 1.2-b).

1.2. PREVIOUS RESEARCH USING GPR DISPERSIVE WAVES

Many GPR users are not familiar with the phenomenon of guided waves, so they may not recognize guided wave behavior in their data. Van der Kruk, Vereecken, and Jacob (2009) give guidance on how to identify guided waves in

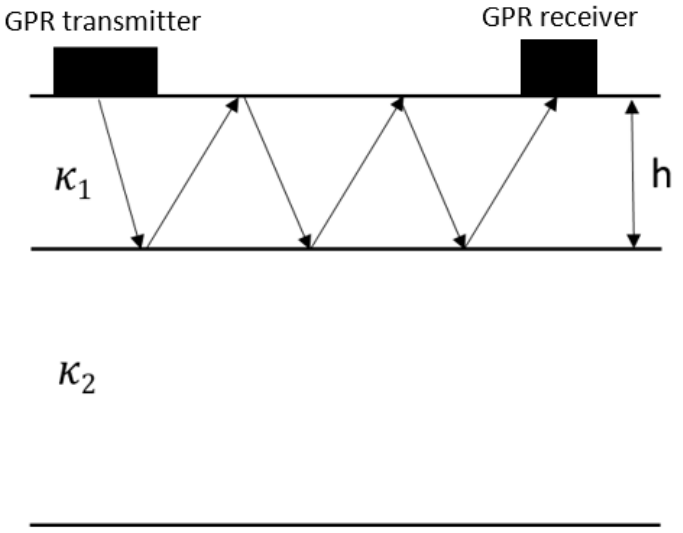

Figure 1.1. Guided waves are trapped within a thin surficial layer. The overlying layer has dielectric permittivity K1 and the underlying layer has dielectric permittivity K2.

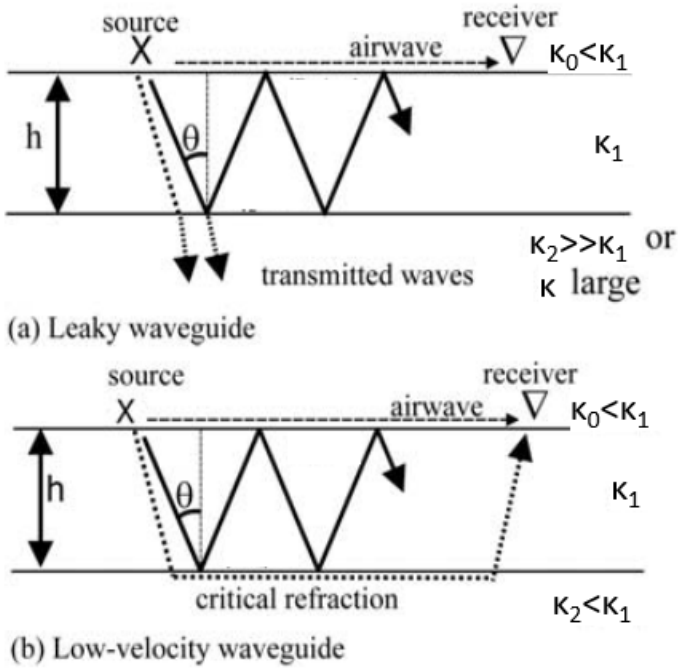

Figure 1.2. Leaky waveguide and low-velocity waveguide (Modified from Van der Kruk et al, 2009).

GPR data and to use these data to estimate the permittivity and thickness of the waveguide layer in this paper. First, in order to show the potential wave phenomenon, the researchers performed three-dimensional FDTD (finite-difference time domain) modeling of the electromagnetic wave propagating at the low-velocity surface waveguide. In the resulting graph (Figure 1.3), the body wave propagating on the ground and the head wave in the waveguide can be clearly seen.

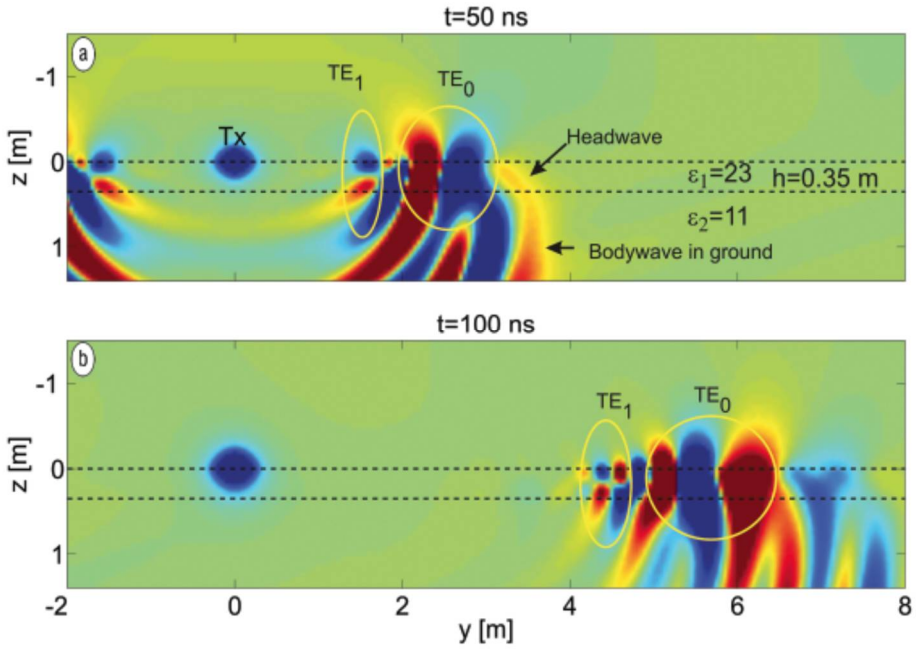

Figure 1.3. The head and body waves in the 3D FDTD modeling electric field, where the yellow circle is the identified TE0 and TE1 modes (Van der Kruk, Vereecken, and Jacob, 2009).

Then, to demonstrate waveguide dispersion in ground-penetrating radar data, a dispersive CMP dataset was collected using a 100-MHz pulseEKKO 100 system on a sediment platform deposit on the braided river. The result (Figure 1.4) shows two main

ways that the dispersive wave can be identified in time-domain GPR data, which is how most GPR data are processed. The first method is to look for “shingles” in the data. In the time domain, dispersive waves often appear as “shingled” energy packets, where a GPR event is characterized by energy packets that occur for relatively short offset spans and are adjacent to each other (Figure 1.4). The second method of identifying dispersion is to observe the length of each energy packet relative to time. Dispersion waves are shown as energy packets that extend over time as the offset increases. In the case of small offsets, the energy packet will occur in a relatively small time window. Due to dispersion, when the offset is large, the energy packet will occur in a longer time window (Figure 1.4). Figure 1.5 investigates the dispersion observed in Figure 1.4 in more detail.

To discern the chromatic dispersion that exists in the GPR data, researchers have given three key features that can be used for identification: 1) The maximum amplitude data for each trace is normalized, which indicates that the dispersion wave contains most of the energy. 2) Different phase and group velocities are indicated by the Shingling reflections. 3) The frequency-dependent phase velocity is clearly indicated by the phase velocity spectrum. The dispersion and inversion properties of GPR data are used in our Experiments, shown in a figure similar to Figure 1.6.

Researchers have used GPR dispersive waves for several different applications, including measuring the water content in near-surface soils, estimating the thickness of frozen soil layers, and estimating the properties of concrete. Some of the earliest work was done to measure the thickness and properties of an ice layer over liquid water.

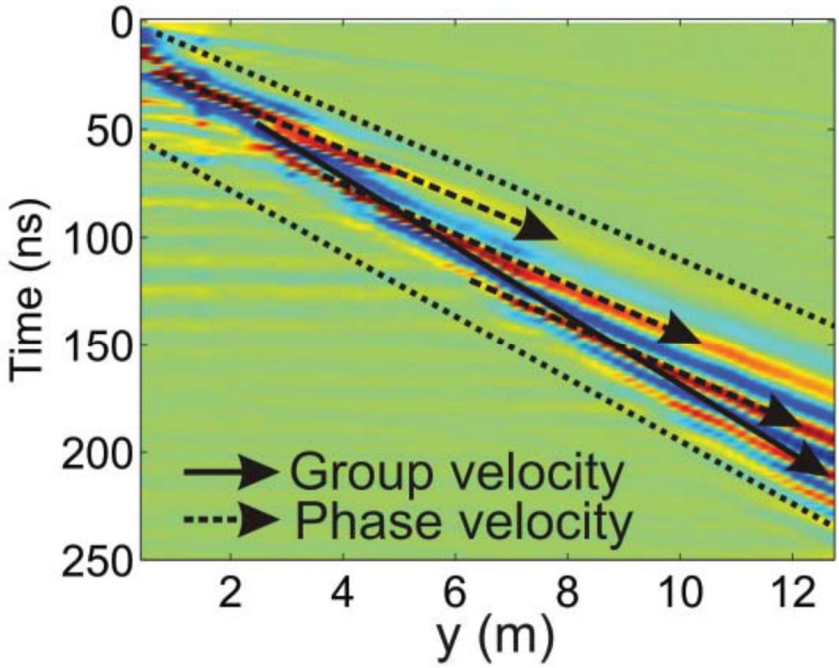

Figure 1.4. The group velocity and phase velocity obtained from the collected CMP data set (Van der Kruk, Vereecken, and Jacob, 2009).

Van der Kruk et al (2007) studied the inversion of the fundamental mode and high mode of the dispersed GPR wave in ice. The same low-permittivity waveguide as the high-permittivity waveguide can also derive the physical properties of the dielectric layer from the scattered guiding GPR pulses. Analysis of the reflection coefficients of TE (broadside) and TM (end-fire) found that the TE mode has less leakage than the TM mode. Therefore, the TE mode is more suitable for inversion when there are more leakage behaviors. In the winter of 2005, researchers collected broadside (TE) and end-fire (TM) data on ice sheets on the lake in Lyme, New Hampshire. The researchers used GSSI System10b with 3101 antennas and 0.1 ns time sampling to obtain several WARR profiles.

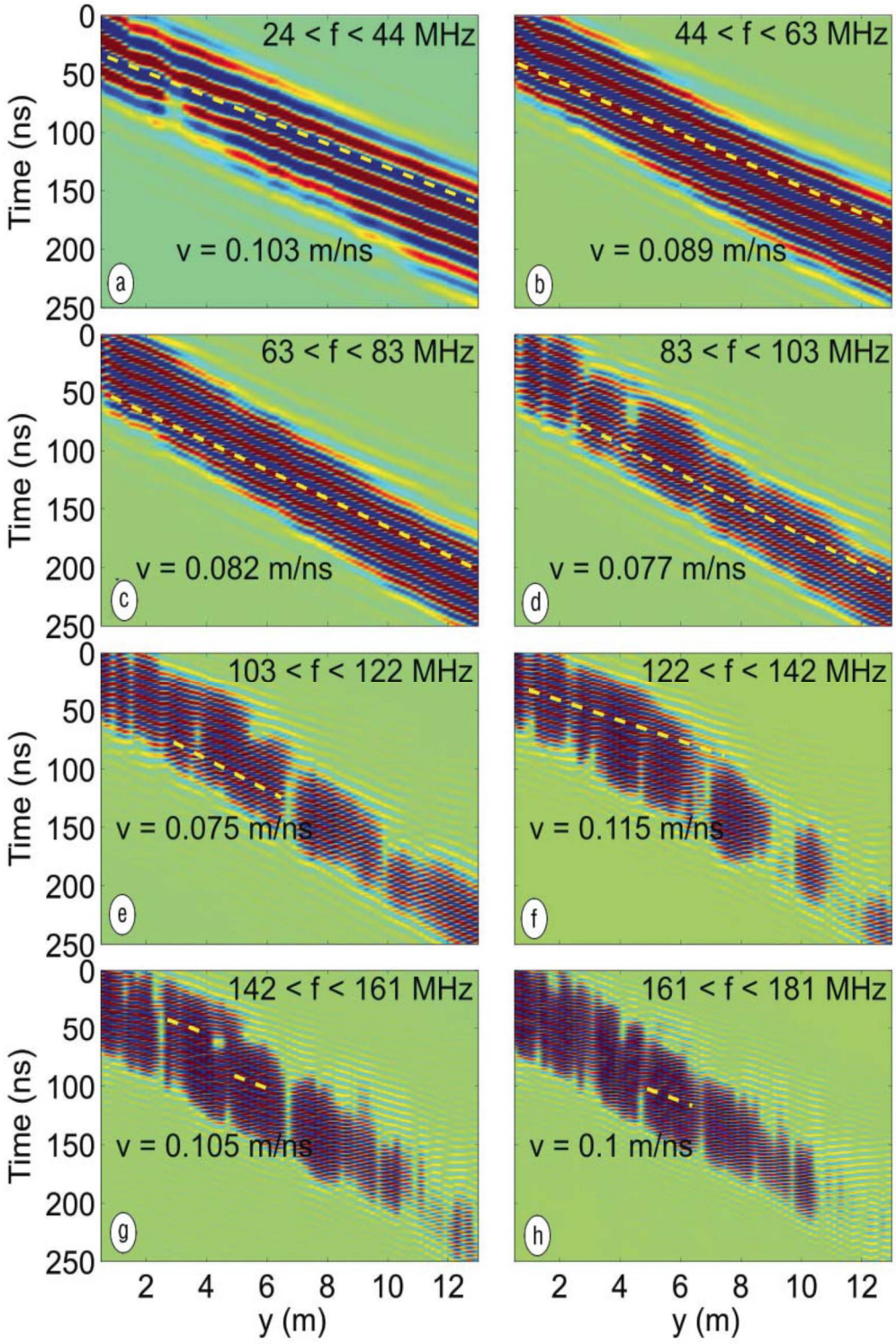

Figure 1.5. Frequency-band analysis of data set for frequency ranges (Van der Kruk, Vereecken, and Jacob, 2009).

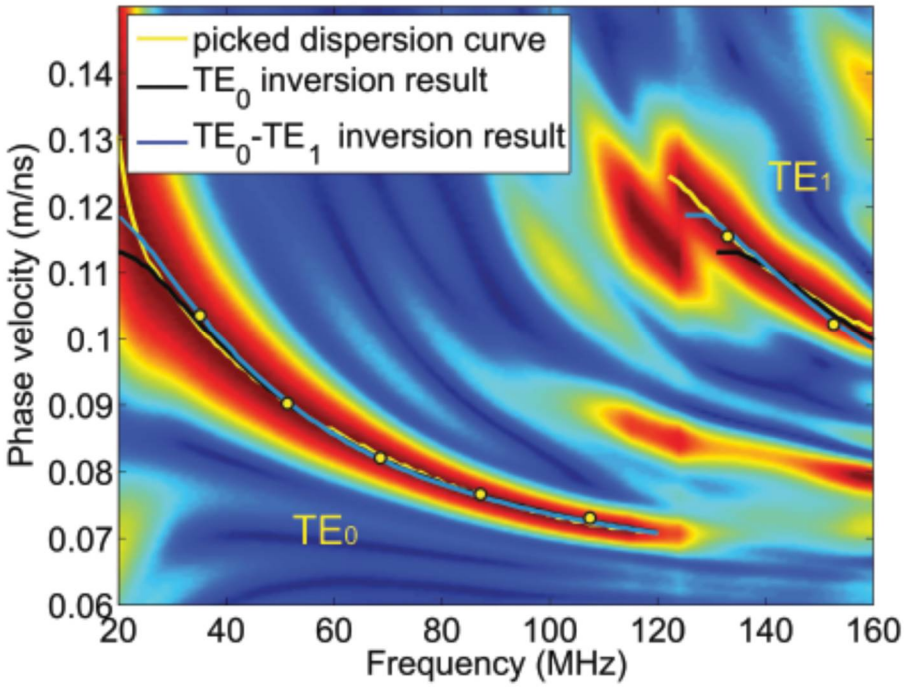

Figure 1.6. Phase velocity spectrum of TE mode data. The red part is high amplitudes and the blue part is low amplitudes. The yellow line is TE0 and TE1 picked dispersion curves, the black line is the inversion result of TE0, and the blue line is the inversion result (Van der Kruk, Vereecken, and Jacob, 2009).

The broadside (TE) data was collected by consequent marking the fixed spacing with 0.05 meters spatial sampling. The end-fire (TM) data is different from the broadside data, which is discretely collected and has a spatial sampling of 0.2 meters. The dispersion curves for TE and TM are selected from the phase velocity spectra of the broadside and end-fire data collected on ice. In addition to the separate measurement and analysis, a combination of the two models was also attempted, but a similar ice thickness was finally obtained. The dielectric permittivity of the ice layer is slightly different. The researchers combined TE1-TE3-TE5 and TM2-TM4-TM6 into TE1-TM2-TE3-TM4-

TE5-TM6 and obtained results consistent with TE1-TE3-TE5. It is considered that the broadside (TE) data is more suitable for studying the medium property of ice.

Van der Kruk et al. (2009) used GPR to characterize the thickness of frozen and thawed soil layers. The high-frequency GPR (greater than250 MHz) is non-invasive and is sensitive to the frozen soil which makes it possible to measure the liquid water content in the soil. These properties make high-frequency GPR suitable for monitoring shallow subsurface (less than 1 meter deep) freezing and thawing processes. Seasonally frozen sand overlain with wet and thawed sand that is then covered with frozen sand can form leaky waveguides and low-velocity waveguides. This allows the permittivity and thickness of the formation to be obtained through phase-velocity and dispersion curves. The researchers used a sensor and software PulseEKKO 1000 GPR system with a 900 MHz bistatic antenna to collect common midpoint gathers at a site near Waterloo, Ontario, Canada. For leaky waveguide, compared to the separate inversion for each mode, combining higher order modes has better constraints inversion. Therefore, the researchers combined the TE3, TE5, TE7, and TE9 modes they identified and inverted the combined TE3-TE5-TE7-TE9. Researchers believe that fitting the TE7 model is more important than fitting the TE3, TE5, and TE9 modes because the maximum value of the effective spectrum is about 800 MHz. For low-velocity waveguide, the combined inversion of TE and TM data provides better results than the separate TE or TM inversion. Therefore, the researchers combined and inverted TE0-TM0, which fits well with the dispersion curve. The method of obtaining the waveguide characteristics by inverting the dispersion curve can better monitor the freezing and thawing process of the near surface, glaciers, ice margins, and frozen ground. This paper uses the same data

analysis method of waveguide dispersion inversion as our Experiment to study the freezing and thawing process of soil.

Xiao et al. (2015) developed a new method for characterizing concrete structures with water gradients using the dispersion of EM (Electromagnetic) waveguides. Figure 1.7 shows the configuration used by the researchers, which was developed by the EM leaky waveguide model. This configuration can be used for the propagation of EM waves in a double layer waveguide. It lays two layers of media on an ideal electrical conductor or water to correspond to an increase in water content in the concrete structure. In this paper, the authors use the guided propagation of EM waves generated by this two-layer medium as a horizontal plane layer.

To verify this procedure, the researchers selected two non-destructive materials for the Experiment: PVC and limestone. In order to form a waveguide medium, these two materials are placed on a metal plate. Researchers used the SIR-3000 GPR system in combination with two 2.6 GHz antennas to acquire TE antenna polarized CMP radars The researchers inverted the collected data and concluded that the combination mode of the two or three modes is better than the reversal of the single mode in the inversion process.

It also confirmed that this model has a simplified effect on the thickness and dielectric properties of the layered material. They conducted further Experiments using GPR with concrete during the capillary absorption process to compare the influent depth and water content gradient. Figure 1.8 shows the apparatus used in the concrete Experiment.

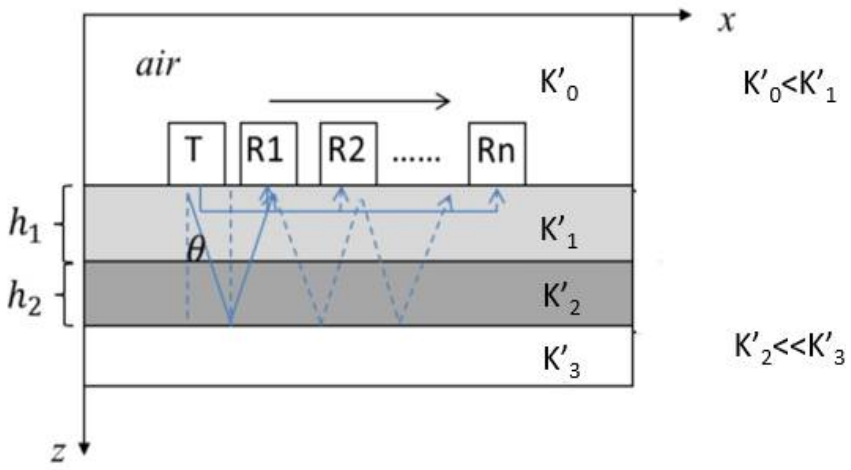

Figure 1.7. The configuration used by the researchers, which was developed by the EM leaky waveguide model (Modified from Xiao et al., 2015).

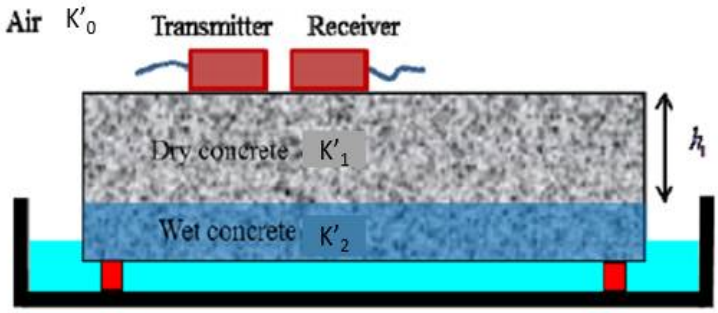

Figure 1.8. The apparatus used in the concrete Experiment. (Modified from Xiao et al., 2015).

The authors also found EM leaks at the interface between concrete and water and can be considered electrical conductors. They concluded that the EM waveguide dispersion method can be used to monitor water content changes in concrete structures.

Rege and Godio (2010) propose a new method to invert the dispersion curve based on the value assumed by the function describing the propagation mode. To validate this method, they analyzed synthetic data and two sets of real GPR data obtained through

WARR (wide angle reflection and refraction). The first set of field data was collected in Montemezzo site, Lombardy, Italy, which was covered with moist soil on dry bedrock. The Experiment uses a TE configuration and both antennas have a main frequency of 100 MHz (Figure 1.9).

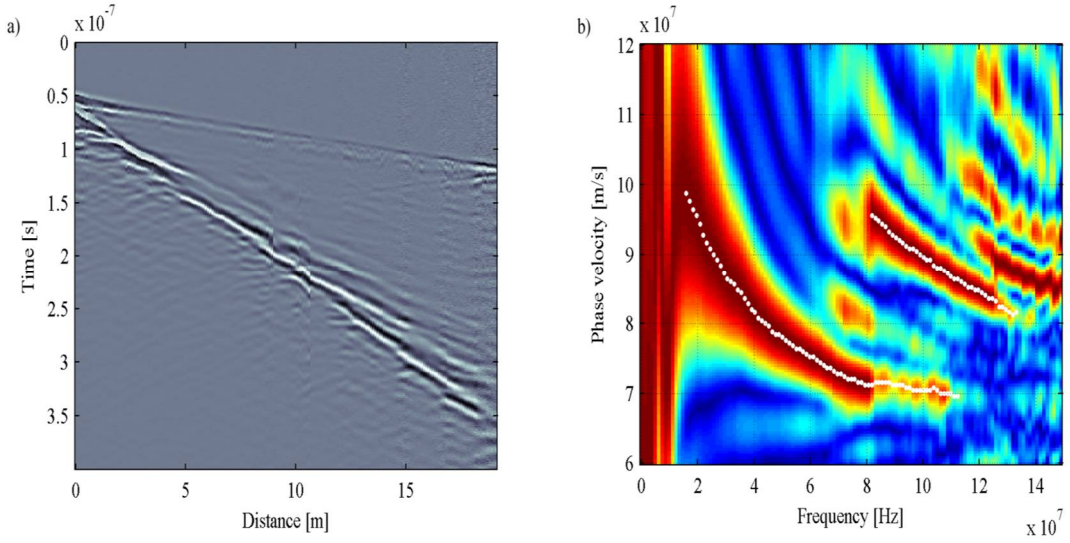

Figure 1.9. Radargram (a), phase velocity spectrum and selected dispersion curve (b) for TE configuration obtained at the Montemezzo test site (Rege and Godio, 2010).

The second set of field data was collected at the Valtournache-Cervinia site in Aosta Valley, Italy which had approximately 0.52 – 0.56 meters of snow on the ground. A TE configuration was also used with a 100 MHz transmitter and a 200MHz receiver. Both datasets were analyzed using the author's proposed method of detecting permittivity and estimating layer thickness and the practicability of the method was proved by comparing the obtained dielectric constant and layer thickness (Figure 1.10 and Figure 1.11).

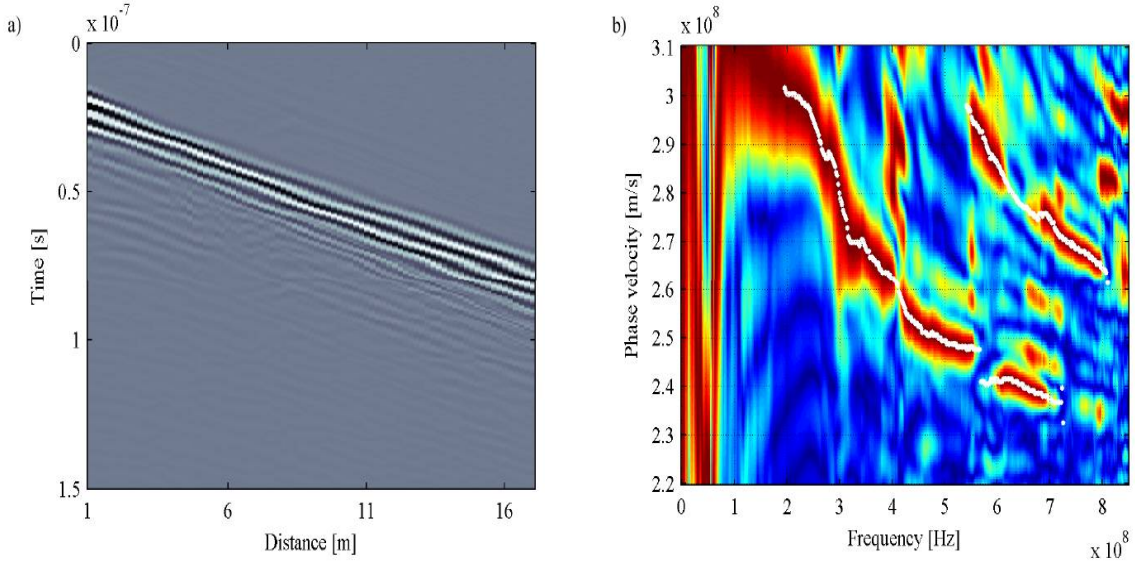

Figure 1.10. Radargram (a), phase velocity spectrum and selected dispersion (Rege and Godio, 2010).

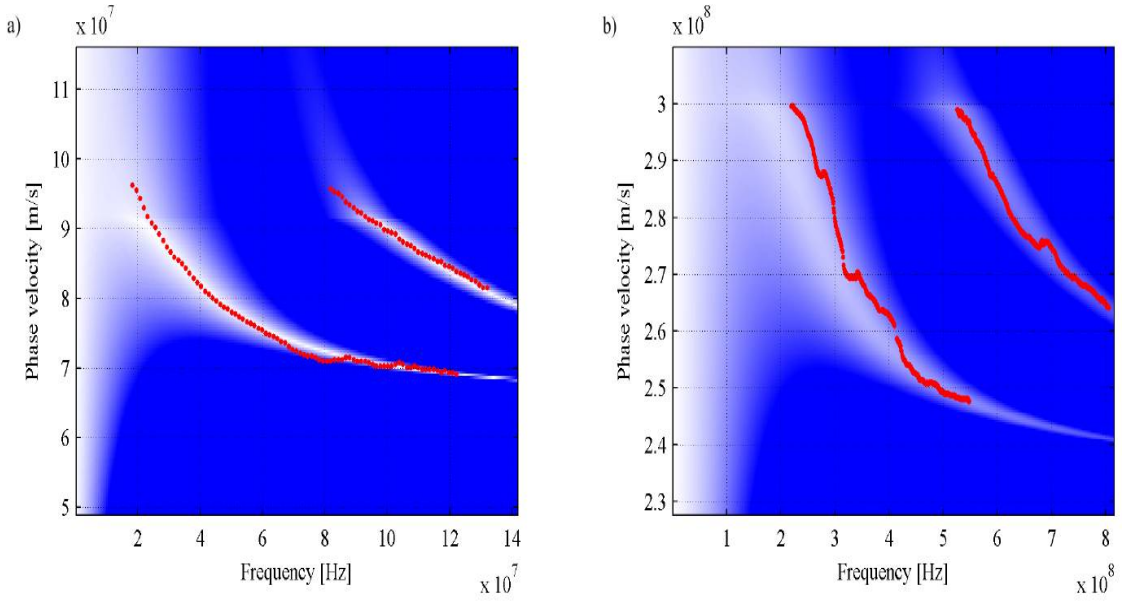

Figure 1.11. Misfit function of the inverted profile of the Montemezzo site (a) and Cervinia site (b) (Rege and Godio, 2010).

2. METHOD

This part mainly introduced the data acquisition and data processing, more details were concluded by Dr. Hajiani in his 2016 research.

2.1. DATA ACQUISITION

The data acquisition part is a brief summary of the article-identifying shallow subsurface stratigraphy and voids using dispersive characteristics of electromagnetic and surface waves (Hajiani, 2016). This project has of six Experiments; with all data acquired under different layer thickness, dielectric permittivity, GPR frequency, and soil texture. Soil textures are dry sand, wet sand, dry organic loam, wet organic loam, dry silt, and wet silt. All Experiments were taken within an Experimental tank, the size of the tank is 3.7 m x 2.4 m x 1.2 m (Figure 2.1). The material of tank is high strength fiberglass. A metal component was not used because metal will affect the GPR wave propagation**.** All Experiments have a base layer with constant thickness in either dry or saturated conditions. Layers with water content for each soil type aim to create an environment for guided waves. A thin rubber tarp was laid over the base layer to serve as a hydraulic barrier between the basal layer and overlying layers. An overlying soil layer with contrasting soil moisture (compared to the base layer) was placed over the tarp. The initial thickness of the overlying layer was 3 cm, this is the thinnest thickness that can be placed to ensure that the layer is level and uniform. Additional 3 cm soil layers were added in increments throughout the Experiment. Each layer thickness acquires four frequencies of GPR profiles. For Experiment 1, the base layer used homogenously saturated sand, and the overlaying layers used completely dry sand. For Experiment 2, the

base layer used dry sand and the overlaying layer used saturated sand. For Experiment 3, the base layer used saturated organic loam; and the overlaying layer used dry organic loam. For Experiment 4, the base layer used using dry organic loam; and the overlaying layer used saturated organic layer. Similarly, Experiment 5 used saturated silt as the base layer and dry silt as the overlaying layer. Experiment 6 used dry silt as the base layer and saturated silt as the overlaying layer.

2.1.1. Soil Preparation. Soil water content can influence the dielectric permittivity of soils. However, creating uniform permittivity soil layers requires careful control of soil water. Only using very wet or very dry soil is recommended for creating soil layers with homogeneous water content. To create dry soil, each soil type needs to be placed in a drying oven for 24 hours at 110°C to make sure all pore water is removed. Because the amount of soil exceeded the maximum capacity of drying, the dry soil was stored in air-tight drums until all soil completed the drying process. For making saturated soil (very wet soil), it is necessary to determine the initial water content of the soil. After determining the initial water content of the soil, place measured quantities of soil and water in a mechanical mixer and for mixing then check the status of water saturation and add additional water when necessary. After the mixing process, soil should have a uniform volumetric water content that was close to saturation. Each time using the mixer, the volumetric water content needs to be calculated to verify the homogeneity of the saturation. Water content weight and soil density were acquired from the saturated soil. Saturated soil was stored in air-tight drums until there was enough for all Experiments.

2.1.2. Soil Placement. Carefully put the soil in the tank to make sure the constant thickness throughout the tank. Acquiring GPR profile after each fill of soil. When the base soil

layer was saturated, and the overlying layers were dry, a 0.4mm plastic sheet was placed over the based layer and pinned on sides of the tank to keep water from escaping the layer. Dry soil was then placed in layers on the plastic sheet. When the base soil layer was dry, and the overlying layers were saturated, a 1.1 mm rubber liner was placed over the dry soil to make sure no water seeped into the dry base. According to preliminary studies, both plastic sheet and rubber liner shows no effect to electromagnetic wave transmission. The plastic sheet was easy to fit to the shape of the tank and was enough to stop the upward migration of water. A thicker rubber liner was required to stop downwards drainage from saturated soil layers which constructed on top of it.

2.1.3. GPR Data Acquisition Parameters. Acquisition of GPR data using pulseEKKO Pro system including sensors with 100, 250, 500, and 1000 MHz antennas and software. Three variable-offset surveys took in 100, 250,500 and 1000MHz frequencies after each soil layer was placed. For this research, only results for the CMP surveys were analyzed. When using 250, 500, and 1000 MHz antennas, the transmitter and receiver were placed in the center of the tank at first, then were slowly moved separately. A similar process was used for the 100 MHz antennas, but the initial antenna offset was 100 cm. For the variable-offset survey, spatial sampling interval for 100 MHz antennas was 10cm, for 250 MHz antennae was 2 cm, for 500 MHz antennae was 2 cm, and for 1000MHz antennas was 1cm**.** Antennas were moved remotely to prevent compacting soil (Figure 2.1).

2.1.4.Monitoring Soil Water Content. Six 7.5 cm long time domain reflectometry (TDR) probes were installed around the tank (two stations on the long edge and one station at the shorter edge) to monitor the dielectric permittivity in each layer of

soil, as shown by the vertical cables in Figure 2.1. In each station, TDR probes were placed horizontally with a 6cm vertical interval. For neighboring soil layers, the installation of the probes at different stations was staggered in depth. TDR data were acquired using an automated TDR system with 14 multiplexers connected to a Campbell Scientific TDR100 reflectometer and datalogger. Data was acquired once an hour. Due to the different situation between each Experiment, the number of TDR probes placed in the base layer may vary. When the base layer is saturated, three probes will be buried in the saturated base layer for each TDR station. When the base layer is dry, numbers of TDR placed in the base layer will reduce. Because the permittivity of dry soil does not change through time, and TDR cables were serving as potential conduits of leaks. Six probes were placed 3 cm below the rubber liner to detect leakage. The TDR probes showed that the permittivity changed very little throughout each Experiment and that the permittivity was mostly homogeneous within each soil unit. The TDR probes helped to ensure that the water content (and thus the electromagnetic velocity) of the soil remained constant throughout the Experiment. The TDR probes also provided “ground truth” for the permittivity of each layer.

Additionally, each soil layer will collect at least two water content samples in the middle of the tank. This measurement will include both the soil placing period and soil excavating period. Samples from the middle of the tank do not show water content change over the duration of the Experiment. Since permittivity closely relates to water content, if the gravimetric water content is consistent, the permittivity in each layer is uniform during the Experiment as shown as TDR data.

Figure 2.1. The Experimental tank was constructed with no metal and filled with horizontal layers of soil. In this figure, 250 MHz antennas are being moved over dry sand.

2.2. DATA PROCESSING

Data processing part also summarized from Dr. Hajiani's research.

2.2.1. Waveguide Model and Theoretical Dispersion Curve. The obtained Experimental data were processed by a method developed by Jan van der Kruk et al. (2006). According to modal theory, incident energy can form a number of modes consisting of specific frequencies associated with waveguide characteristics. These modes travel at their own phase velocity within the dispersive waveguide. When the thickness of the waveguide layer is (h), the equation can be written as:

$$1 - \widehat{R}_{12}^{\{TE,TM\}}(\theta)\widehat{R}_{10}^{\{TE,TM\}}(\theta)\exp[-2\hat{\gamma}_1 h\cos(\theta)] = 0 \quad (1)$$

This equation gives the conditions in which guided waves are present. In this equation, ˆ indicate frequency dependent variable, $\widehat{R}_{10}^{\{TE,TM\}}$ and $\widehat{R}_{12}^{\{TE,TM\}}$ represent the reflection coefficients at the upper and lower boundaries of the waveguide, respectively, h is the thickness of the waveguide, θ is incidence angle, and $\widehat{\gamma_1}$ is propagation constant that GPR waves traveling through the waveguide. For the lossless case and μ = μ0 (μ is permeability)

$$\widehat{\gamma_a} = j\omega\sqrt{\varepsilon a}/c_0 \tag{2}$$

where ε_a is the relative permittivity of medium a, c_0 is the velocity of light in a vacuum, and ω is the angular frequency (Figure 2.2).

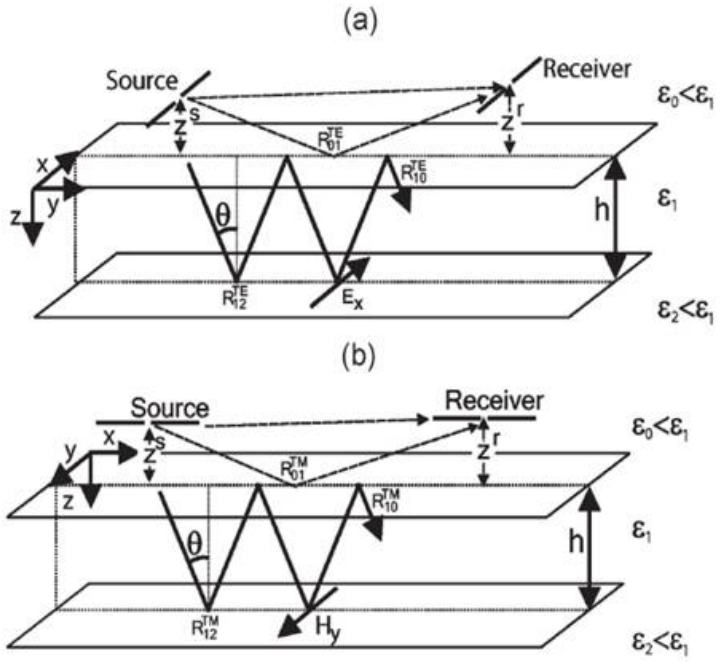

Figure 2.2. Diagram of (a) the TE and (b) TM source-receiver configurations. For both configurations, the x-axis is oriented parallel to the long axes of the antennas. ε_0, ε_1, and ε_2 are the relative permittivities of the respective media. $R_{a,b}^{TE,TM}$ is the reflection coefficients for TE- and TM- mode GPR wages incident at the boundary between the a and b media (Van der Kruk, 2006).

The reflection coefficients at the upper and lower boundaries of the waveguide are given by:

$$\hat{R}_{10}^{TE} = \frac{\hat{\Gamma}_1 - \hat{\Gamma}_0}{\hat{\Gamma}_1 + \hat{\Gamma}_0} \tag{3a}$$

$$\hat{R}_{10}^{TM} = \frac{\hat{\gamma}_1^2\hat{\Gamma}_0 - \hat{\gamma}_0^2\hat{\Gamma}_1}{\hat{\gamma}_1^2\hat{\Gamma}_0 + \hat{\gamma}_1^2\hat{\Gamma}_1} \tag{3b}$$

$$\hat{R}_{12}^{TE} = \frac{\hat{\Gamma}_1 - \hat{\Gamma}_2}{\hat{\Gamma}_1 + \hat{\Gamma}_2} \tag{3c}$$

$$\hat{R}_{12}^{TM} = \frac{\hat{\gamma}_1^2\hat{\Gamma}_2 - \hat{\gamma}_2^2\hat{\Gamma}_1}{\hat{\gamma}_1^2\hat{\Gamma}_2 + \hat{\gamma}_2^2\hat{\Gamma}_1} \tag{3d}$$

Where $\hat{\Gamma}_a = \sqrt{\hat{\gamma}_a^2 - \hat{\gamma}_1^2 \sin^2(\theta)}, \quad (a = 0, 1, 2) \text{ with } \mathrm{Re}(\hat{\Gamma}_a) \geq 0$ (4)

There are two requirements for Equation (1): First, the reflection coefficient at each interface must be satisfied to have an amplitude equal to one. To achieve this, θ must exceed the critical angle (θc), depending on the dielectric constant of the waveguide (ε_1) and lower (ε_2) layers.

$$\theta c = \sin^{-1}\left(\sqrt{\frac{\varepsilon_2}{\varepsilon_1}}\right) \tag{5}$$

The total phase change after continuous reflection at the upper and lower interfaces must be equal to 2mπrad, where m is an integer, which is the second requirement to be met. The different values of m correspond to different guided wave modes. The value of the basic mode is m = 0. By substituting (2) in (1) and analyzing its phase component φ, the formula can be written:

$$\phi^{\{TE,TM\}}(\theta) - \frac{4\pi f\sqrt{\varepsilon_1}h\cos(\theta)}{c_0} = -2m\pi \tag{6}$$

where

$$\phi^{\{TE,TM\}}(\theta) = \tan^{-1}\left(\frac{\mathrm{Imag}\,(\hat{R}_{10}^{\{TE,TM\}})}{\mathrm{Real}\,(\hat{R}_{10}^{\{TE,TM\}})}\right) + \tan^{-1}\left(\frac{\mathrm{Imag}\,(\hat{R}_{12}^{\{TE,TM\}})}{\mathrm{Real}\,(\hat{R}_{12}^{\{TE,TM\}})}\right) \tag{7}$$

Jan van der Kruk (2007) uses the zero-search procedure of the model parameters ε_1, ε_2 and h to solve θ in equations (1) and (6). The phase velocity v of the frequency f is:

$$v(f, \varepsilon_1, \varepsilon_2, h) = \frac{c_0}{\sqrt{\varepsilon_1}\sin[\theta(f,\varepsilon_1,\varepsilon_2,h)]} \tag{8}$$

where c_0 is the velocity of light in a vacuum, f is frequency, ε_1 is permittivity of the waveguide, ε_2 is permittivity of the lower space, h is waveguide thickness. It can be seen from equations (1) and (8) that as the frequency increases, θ will increase and the phase velocity will decrease.

2.2.2. Determination of Phase Velocity Spectrum from CMP Data. Firstly, convert the offset time domain into an offset frequency domain by Fourier transform:

$$\hat{U}(x, f) = \int U(x, t)\, e^{-i2\pi ft} dt \tag{9}$$

where x is offset, f is frequency, and t is time, $\hat{U}(x, f)$ is the offset-frequency domain, and $U(x, t)$ is the offset-time domain. The offset frequency domain can then be written as the product of the phase spectra and amplitude spectra,

$$\hat{U}(x, f) = \hat{P}(x, f) \times \hat{A}(x, f) \tag{10}$$

where $\hat{P}(x, f)$ is phase spectrum, and $\hat{A}(x, f)$ is amplitude spectrum (Park et al., 1998).

$$\hat{U}(x, f) = e^{-i\Phi x}\ \hat{A}(x, f) \tag{11}$$

where $e^{i\phi x}$ is phase spectrum term

$$\Phi = f/v \tag{12}$$

In order to obtain the function $\hat{W}(f, \varphi)$ of the frequency domain phase wave field, the following integral transformation is applied to $\hat{U}(x, f)$ in equation (8):

$$\hat{W}(f, \varphi) = \int e^{i\varphi x} \frac{\hat{U}(x,f)}{|\hat{U}(x,f)|} dx = \int e^{-i(\phi-\varphi)x} \frac{\hat{A}(x,f)}{|\hat{A}(x,f)|} dx \tag{13}$$

where f is frequency component, φ is offset-dependent phase. The integral transformation in the equation (13) is the summation of the offset of the wave field of the frequency after the offset-dependent phase shift determined for the assumed phase velocity is applied to the wavefield in Equation (11).

Since the dispersion wave propagates at a frequency-dependent phase velocity, the phase change $\Delta\varphi$ of each frequency as a function of the offset variation Δx can be written as:

$$\Delta\phi = \frac{-2\pi f}{v}\ \Delta x \tag{14}$$

where $\Delta\phi$ is phase change, v means phase velocity, Δx means offset change, f is frequency component, and φ is offset-dependent phase.

Accordingly, the maximum value of $\widehat{W}(f,\varphi)$ can be obtained when the following criteria are satisfied in Equation (14):

$$\varphi = \phi = 2\pi f/v \tag{15}$$

Constructive interference occurs when the frequency travels at a specific phase velocity by applying a corresponding phase correction to the frequency and phase velocity. The phase velocity spectrum D(v,f) of the selected frequency range and phase velocity can be obtained:

$$D(v,f) = \left|\sum_x \frac{\hat{E}(x,f)}{|\hat{E}(x,f)|}\exp\left(i\frac{2\pi f}{v}x\right)\right| \tag{16}$$

where D(v,f) is the phase-velocity spectrum, E(x,t) is the CMP data depending on the offset, x, of the antennas and time t, $\hat{E}$ (x,f) is the CMP data E(x,t) transformed to the frequency domain, v is the phase velocity, f is frequency, i is the square root of -1.

By choosing the maximum value for each TE mode to obtain a dispersion curve showing the phase velocity as a function of frequency, the formula can be written as:

$$v_{data}(f) = \max[D(v, f)] \tag{17}$$

The phase velocity of each frequency component is determined by the maximum value of the wavefield in the frequency-phase domain. The dispersion curves of phase velocity and frequency are constructed by these maximum values.

2.2.3. Inversion of Dispersion Curve. According to van der Kruk (2009), these dispersion curves form the basis of the processing tools used to interpret the dispersive GPR data. The following Formula can be obtained by using the curves selected by the TE0 and TE1 modes for inverting the dielectric properties of the waveguide and the half space below, using a similar technique developed by the seismic community, and involving minimizing the cost function:

$$C^{TE_m}(\boldsymbol{\varepsilon_1}, \boldsymbol{\varepsilon_2}, \mathbf{h}) = \sum_{\mathbf{i=1}}^{\mathbf{n}} \frac{\left|\mathbf{v}_{\mathbf{data}}^{\mathbf{TE_m}}(\mathbf{f_i}) - \mathbf{v}^{\mathbf{TE_m}}(\mathbf{f_i}, \boldsymbol{\varepsilon_1}, \boldsymbol{\varepsilon_2}, \mathbf{h})\right|}{\mathbf{n}} \tag{18}$$

where f_i is the range of i=1. . .n frequencies, $v_{data}^{\{TE_m\}}$ is the picked dispersion curve, and $v^{\{TE_m\}}$ is the calculated theoretical TE_m dispersion curves for a range of models.

2.2.4. Use MATLAB to Processing Data. In this study, data processing was performed using the MATLAB code developed by Van der Kruk et al. (based on seismic dispersive wave methods developed by Park et al. (1998)). Using this software, I selected the dispersion curve, then inverted it to obtain surface waveguide characteristics.

3. RESULTS

The purpose of this study was to investigate how changing the allowable velocity range when analyzing guided wave data will affect the results of estimating the dielectric permittivity and thickness of each layer in a controlled environment. To test our hypothesis, we chose Experiment 3, Experiment 4, Experiment 5, and Experiment 6 to conduct a comparative study and perform three exercises for each frequency based on the GPR antenna frequencies of 250 MHz, 500 MHz, and 1000 MHz. Even though 100 MHz data were acquired, we did not compare the 100 MHz data because dispersive waves were seldom observed for this frequency. Dispersive waves were likely unable to form for the 100 MHz data because the limited size of the tank did not allow data to be collected at the longer offsets needed for guided waves to form at this lower frequency. Also, the layers in the tank were not sufficiently deep for guided waves to form at the 100 MHz frequency. Experiments 1 and 2 were excluded from the study because too few soil layers were used, so the data sets were not comparable to the other Experiments.

Two variables are considered at the beginning of each Experiment: phase velocity and frequency. For phase velocity, we experimented with three different phase velocity ranges. The first velocity range considered was greater than 0.2 m/ns. The second range included all data with a velocity greater than 0.15 m/ns and less than or equal to 0.2 m/ns. The third range was all data with velocity less than or equal to 0.15 m/ns. Frequency is determined by the selected phase velocity. To analyze the influence of the starting point more accurately, we used the method of controlling variables. The phase velocity and frequency of the ending point selected for each set of tests were the same. Since there are

three ranges of velocity for the starting point of each frequency, we processed the data for each frequency three times for each soil layer. Both Experiment 3 and Experiment 4 were conducted using organic loam. Experiment 3 used saturated organic loam as the base layer, covered by dry organic loam. Experiment 4 was the foundation of dry organic loam covered by an incremental layer of saturated organic loam. Similarly, both Experiment 5 and Experiment 6 were conducted using silt. Experiment 5 was saturated silt base layer cover by dry silt layer, and Experiment 6 had a dry silt base layer covered with an incremental layer of saturated silt (Table 3.1).

Table 3.1. Materials of each experiment.

Experiment	3	4	5	6
Basal Layer	saturated organic loam	dry organic loam	saturated silt	dry silt
Overlying Layer	dry organic loam	saturated organic loam	dry silt	saturated silt

We chose one example for each of the three different frequencies. Each example contains three sets of dispersive images with different starting points, (a) shows how to select the starting point, and (b) shows the resulting curve of the selected point. Figures 3.1, 3.2, and 3.3 are all selected from Experiment 3 at 250 MHz antennae over 15 cm of dry organic loam overlying wet organic loam. Figure 3.1 shows the dispersion image of starting point is max phase velocity (chosen at 0.35 m/ns, but the actual starting velocity

is 0.3 m/ns). In the resulting graph, the blue dot is the selected point and the green line is the inversion curve. As can be seen from Figure 3.1, the resulting curve fits well with the selected point.

Figure 3.2 shows the dispersion image which starting point is phase velocity at 0.2 m/ns (choose at 0.2 m/ns which actual starting at 0.21 m/ns) at 250 MHz antennae over 15 cm of dry organic loam overlying wet organic loam. The resulting curve in Figure 3.2 also fits well with the selected point.

Figure 3.3 shows the dispersion image that starting point is phase velocity at 0.15 m/ns (chosen at 0.15 m/ns but actual starting at 0.14 m/ns) at 250 MHz antennae over 15 cm of dry organic loam overlying wet organic loam. The resulting curve in Figure 3.3 is longer relative to the selected point, but the trend is the same as the selected point.

Figures 3.4, 3.5, and 3.6 are all selected from Experiment 4 at 500 MHz antennae over 6 cm of wet organic loam overlying dry organic loam. Figure 3.4 shows the dispersion image which starting point is max phase velocity (chosen at 0.35 m/ns but actual starting at 0.35 m/ns). From the resulting graph, it can see that the inversion result is shorter than the picks, but the trend is the same.

Figure 3.5 shows the dispersion image which starting point is phase velocity at 0.2 m/ns (chosen at 0.2 m/ns but actual starting at 0.19 m/ns) at 500 MHz antennae over 6 cm of wet organic loam overlying dry organic loam. The inversion curve in Figure 3.5 fits well with the selected point.

Figure 3.6 shows the dispersion image which starting point is phase velocity at 0.15 m/ns (choose at 0.15 m/ns which actual starting at 0.15 m/ns) at 500 MHz antennae over 6 cm of wet organic loam overlying dry organic loam. Although the inversion curve

in the resulting graph in Figure 3.6 is very similar to Figure 3.5, it can be seen that it varies slightly with different selected points.

Figures 3.7, 3.8, and 3.9 are all selected from Experiment 5 at 1000 MHz antenna over 9 cm of dry silt overlying wet silt. Figure 3.7 shows the dispersion image which starting point is max phase velocity (chosen at 0.35 m/ns but actual starting at 0.35 m/ns). The resulting graph of Figure 3.7 is similar to Figure 3.6. All of them are inversion curves shorter than the selected points, but the inversion curves are in line with most of the picks.

Figure 3.8 shows the dispersion image which starting point is phase velocity at 0.2 m/ns (chosen at 0.2 m/ns which actual starting at 0.225 m/ns) for Experiment 5 at 1000 MHz. The resulting graph of Figure 3.8 is different from the resulting graph of Figure 3.7. It is that the inversion curve is longer than the selected point, but the same is that the curve is consistent with most of the points.

Figure 3.9 shows the dispersion image which starting point is phase velocity at 0.15 m/ns (chosen at 0.15 m/ns but actual starting at 0.17 m/ns) for Experiment 5 at 1000 MHz. Since Figure 3.7, 3.8 and 3.9 have different phase velocities at the starting point, the frequency of the starting point and the phase velocity and frequency of the ending point are the same, and thus that the curves are almost exactly the same.

The following pictures do not have all the velocity ranges, but they are still good data. Figure 3.10 and 3.11 are selected from Experiment 3 at 1000 MHz antenna over 15 cm of dry organic loam overlying wet organic loam. Figure 3.10 shows the dispersion image which starting point is max phase velocity (chosen at 0.35 m/ns but actual starting at 0.32 m/ns).

Figure 3.11 shows the dispersion image which phase velocity starting at 0.2 m/ns (chosen at 0.2 m/ns but actual starting at 0.22 m/ns). Since the minimum observable phase velocity is 0.17 m/ns, there is no data available for the third velocity range, so this group has only two velocity ranges, maximum and 0.2.

(a) (b)

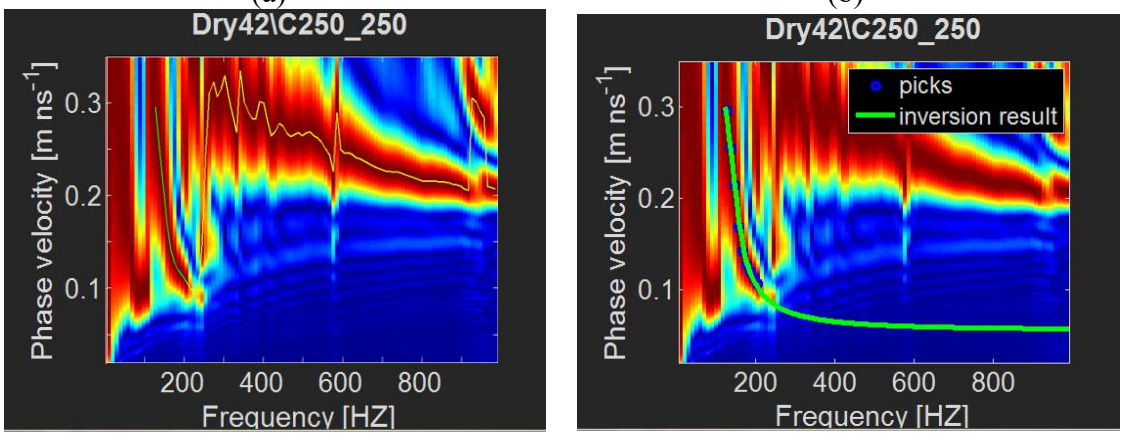

Figure 3.1. Diagram (a) max phase velocity (user selected 0.35 m/ns as the maximum velocity, but the algorithm selected the actual starting velocity as 0.3 m/ns) for Experiment 3 at 250 MHz. (b) Result figure of max phase velocity.

(a) (b)

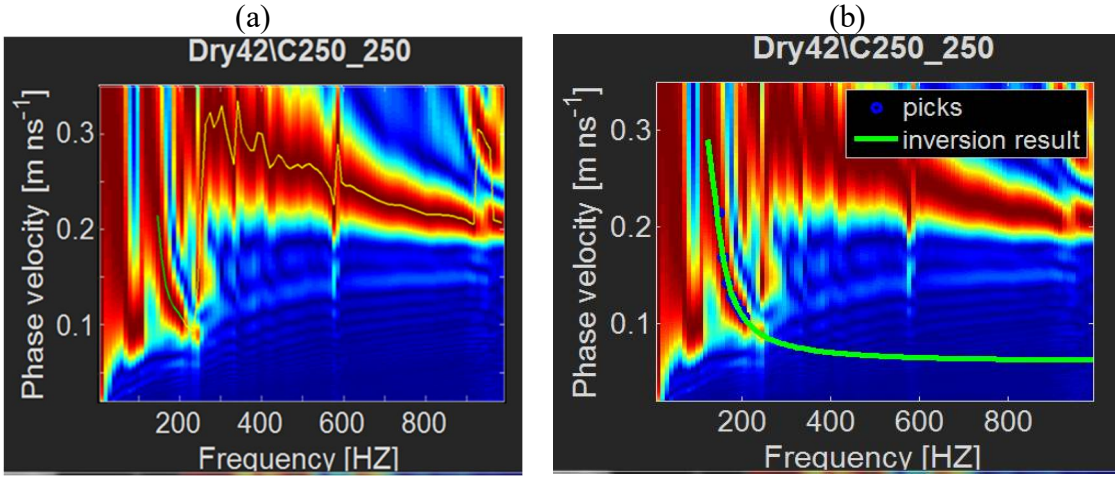

Figure 3.2. Diagram (a) phase velocity starting at 0.2 m/ns (user selected 0.2 m/ns, but the algorithm selected the actual starting velocity as 0.21 m/ns) for Experiment 3 at 250 MHz. (b) Result figure of phase velocity starting at 0.2 m/ns.

(a) (b)

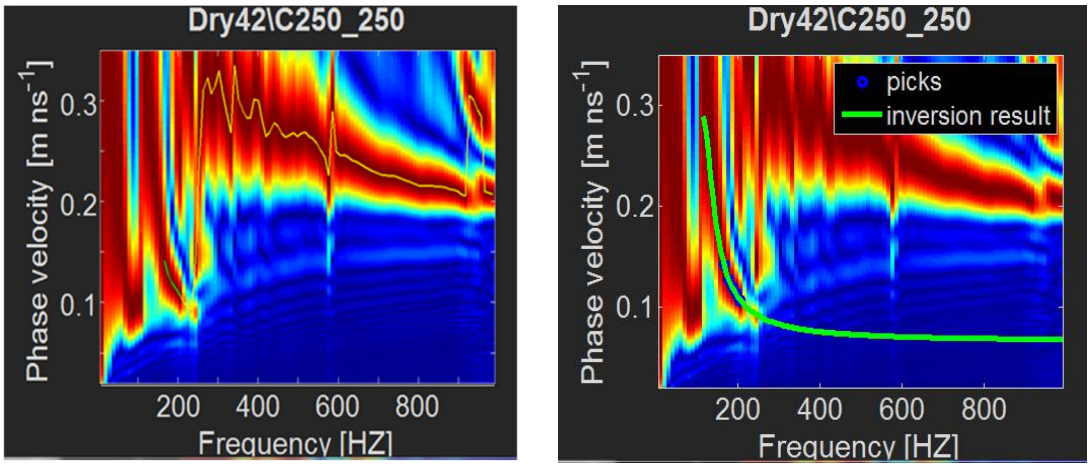

Figure 3.3. Diagram (a) phase velocity starting at 0.15 m/ns (chosen at 0.15 m/ns but actual starting at 0.14 m/ns) for Experiment 3 at 250 MHz. (b) Result figure of phase velocity starting at 0.15 m/ns.

(a) (b)

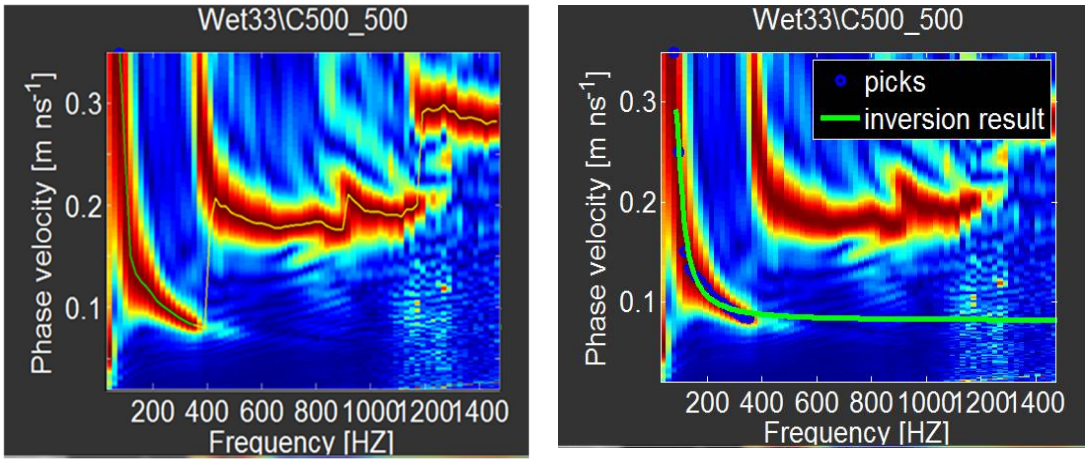

Figure 3.4. Diagram (a) max phase velocity (chosen at 0.35 m/ns but actual starting at 0.35 m/ns) for starting point for Experiment 4 at 500 MHz. (b) Result figure of max phase velocity.

(a) (b)

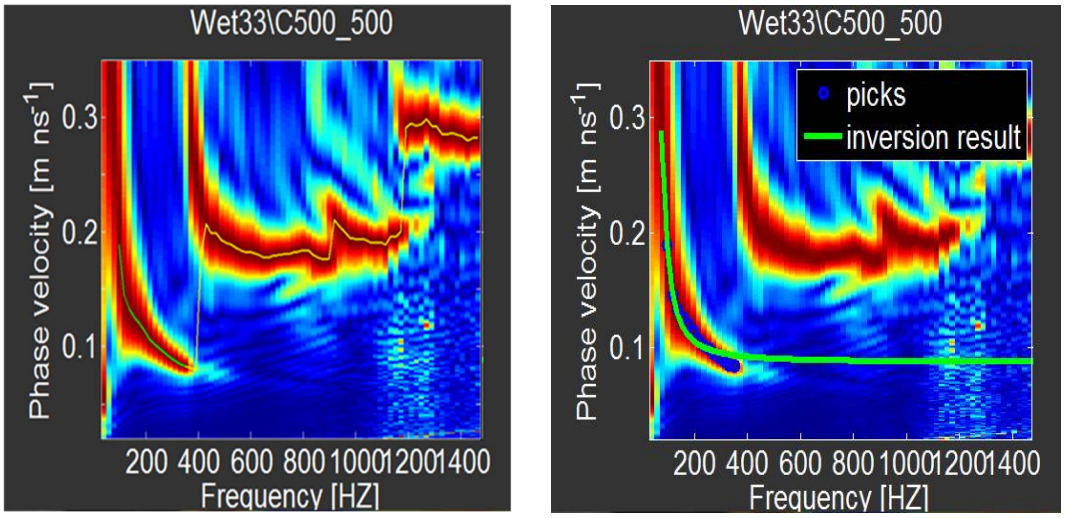

Figure 3.5. Diagram (a) phase velocity starting at 0.2 m/ns (chosen at 0.2 m/ns but actual starting at 0.19 m/ns) for Experiment 4 at 500 MHz. (b) Result figure of phase velocity starting at 0.2 m/ns.

(a) (b)

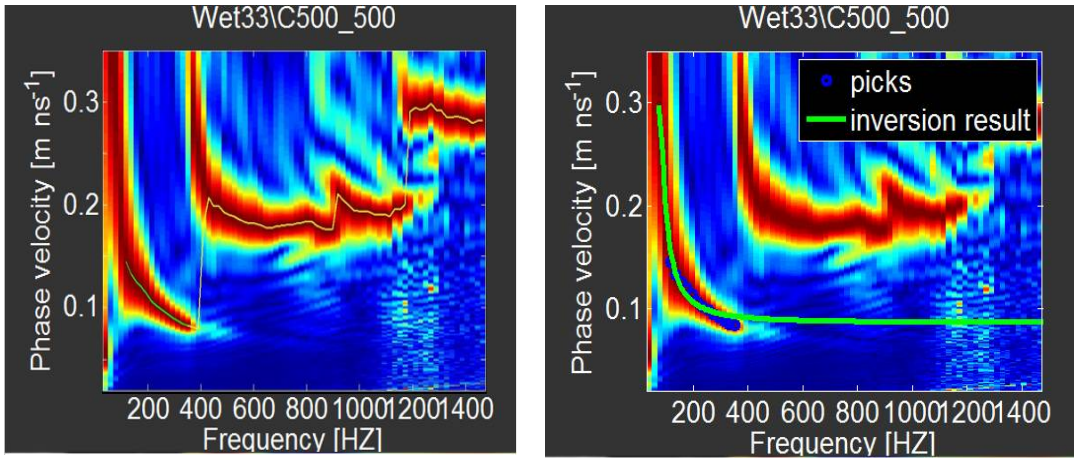

Figure 3.6. Diagram (a) phase velocity starting at 0.15 m/ns (chosen at 0.15 m/ns which actual starting at 0.15 m/ns) for Experiment 4 at 500 MHz. (b) Result figure of phase velocity starting at 0.15 m/ns.

(a) (b)

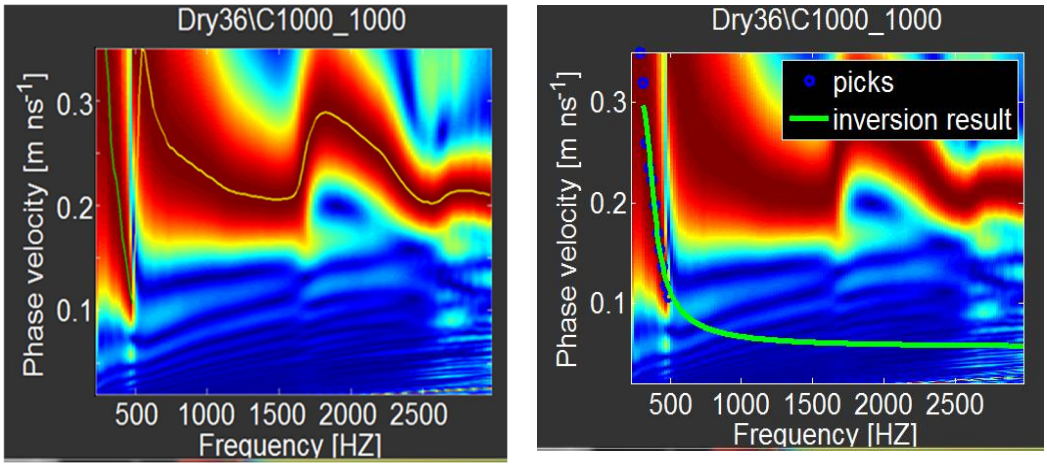

Figure 3.7. Diagram (a) max phase velocity (chosen at 0.35 m/ns which actual starting at 0.35 m/ns) for starting point for Experiment 5 at 1000 MHz. (b) Result figure of max phase velocity.

(a) (b)

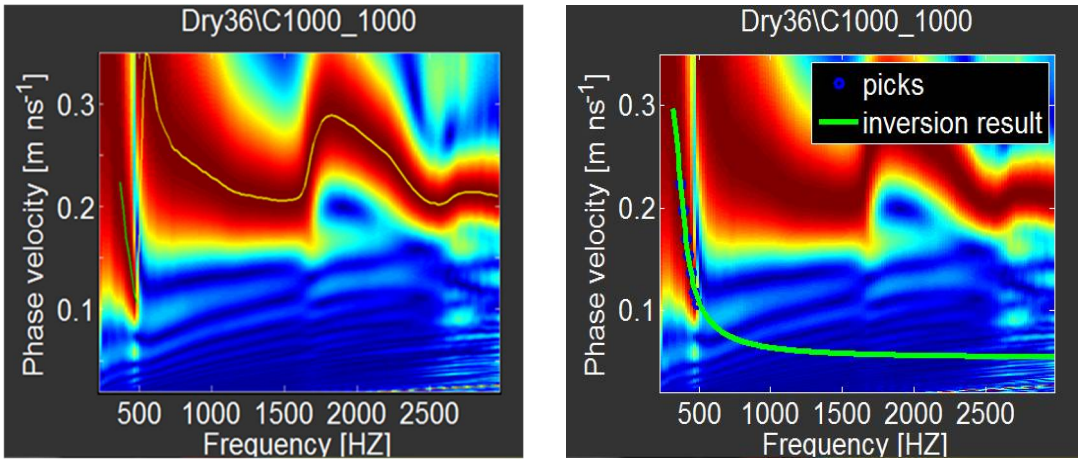

Figure 3.8. Diagram (a) phase velocity starting at 0.2 m/ns (chosen at 0.2 m/ns which actual starting at 0.225 m/ns) for Experiment 5 at 1000 MHz. (b) Result figure of phase velocity starting at 0.2 m/ns.

(a) (b)

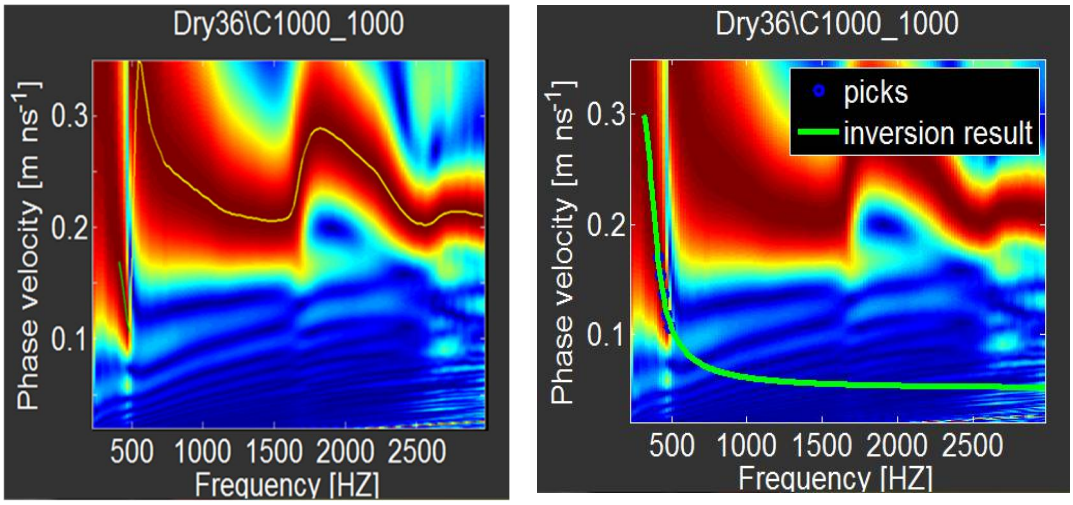

Figure 3.9. Diagram (a) phase velocity starting at 0.15 m/ns (chosen at 0.15 m/ns but actual starting at 0.17 m/ns) for Experiment 5 at 1000 MHz. (b) Result figure of phase velocity starting at 0.15 m/ns.

(a) (b)

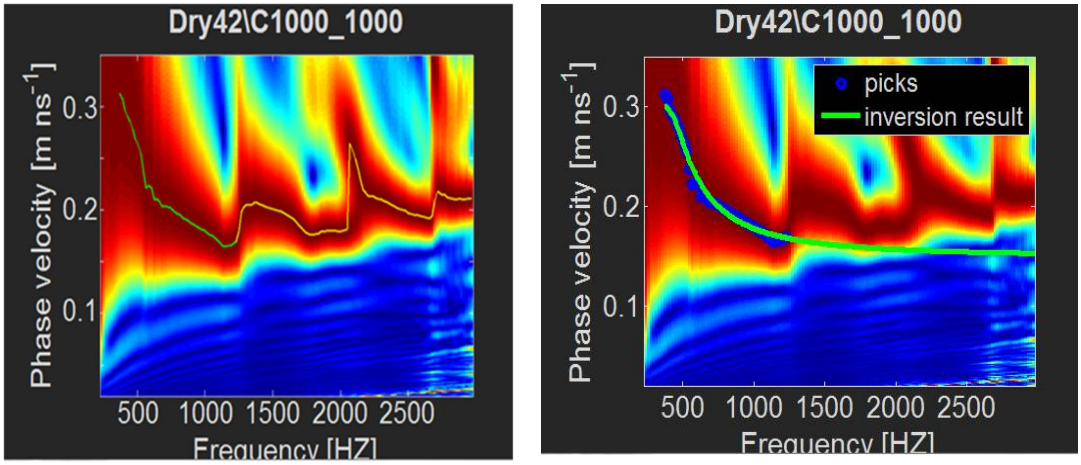

Figure 3.10. Diagram (a) max phase velocity (chosen at 0.35 m/ns but actual starting at 0.32 m/ns) for starting point for Experiment 3 at 1000 MHz. (b) Result figure of max phase velocity.

(a) (b)

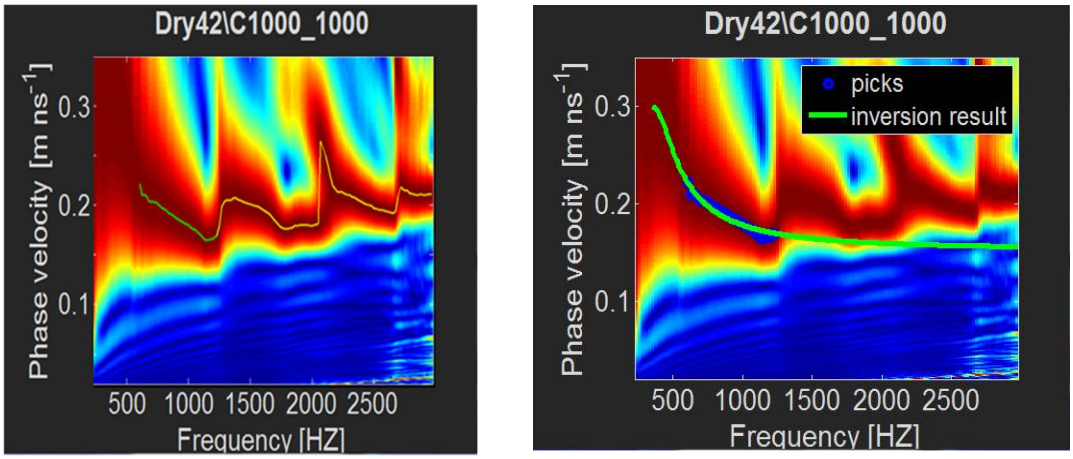

Figure 3.11. Diagram (a) phase velocity starting at 0.2 m/ns (chosen at 0.2 m/ns but actual starting at 0.22 m/ns) for starting point for Experiment 3 at 1000 MHz. (b) Result figure of phase velocity starting at 0.2 m/ns.

4. CONCLUSION

Based on the Experimental data of 'Evaluation of Dispersive GPR Waves for Guided Layer Characterization' (Grote, Hajiani and Alsaaideh, n.d.), the purpose of this study was to investigate how limiting the allowable velocity range when analyzing guided wave data will affect the results of dielectric permittivity and thickness estimation.

In this research, chose Experiment 3, Experiment 4, Experiment 5, and Experiment 6 to conduct a comparative study and perform three surveys for each frequency based on the GPR antenna frequencies of 250 MHz, 500 MHz, and 1000 MHz. The reason did not compare the 100 MHz data is dispersive waves were seldom observed for this frequency and the layers in the tank were not deep enough for the guided wave to form at the 100 MHz frequency. The reason did not compare Experiment 1 and 2 is there are not full data sets for these two Experiments.

Two variables of the starting point are considered at the beginning of each survey: phase velocity and frequency. For phase velocity, we Experimented with three different phase velocity ranges, the first range is phase velocity greater than 0.2 m/ns), the second range is phase velocity greater than 0.15 m/ns and less than or equal to 0.2 m/ns, and the third range is phase velocity less than or equal to 0.15 m/ns. In the following content will use max, 0.2 m/ns, and 0.15 m/ns to represent them. Frequency is determined by the selected phase velocity.

To be able to analyze the influence of the starting point more accurately, the phase velocity and frequency of the ending point selected for each set of surveys were the same. For most of Experiment 3, 5, and 6 there are no data extending down to 0.15 m/ns,

therefore, only compared the starting phase velocity at max (0.3-0.4 m/ns) and 0.2 m/ns for these three Experiments. Experiment 4 has the same data number when choosing all three-phase velocity, so for Experiment 4 compare max phase velocity, 0.2 m/ns, and 0.15 m/ns.

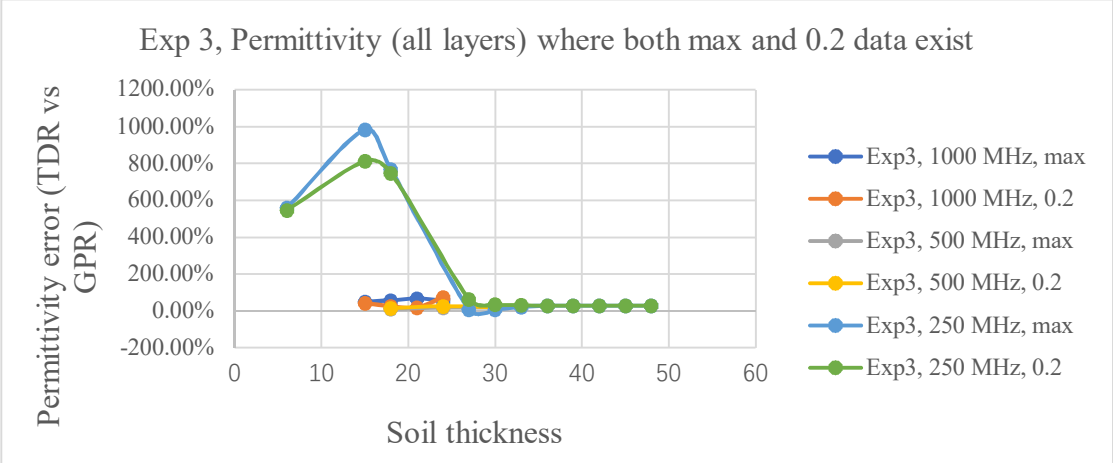

Figure 4.1. Experiment 3, permittivity (all layers) where both max and 0.2 m/ns data exist.

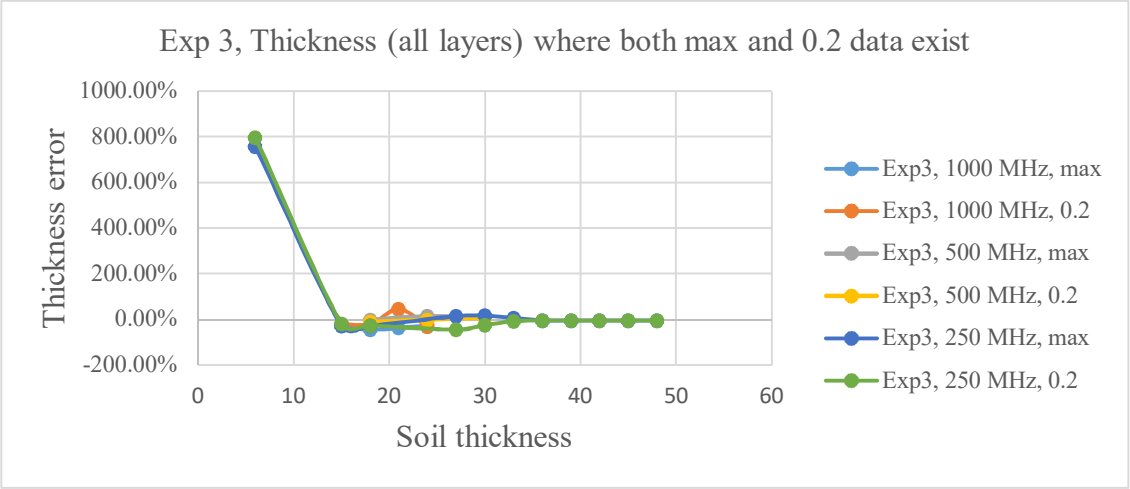

Figure 4.2. Experiment 3, thickness (all layers) where both max and 0.2 m/ns data exist.

Experiment 3 used saturated organic loam as the base layer and covered by dry organic loam. About 1000 MHz data of Experiment 3, for permittivity error (K), thickness error (Z) and error of inversion, choosing phase velocity at 0.2 m/ns give the best results; when frequency is 500 MHz, for permittivity error (K), choosing max phase velocity which is average 0.35 m/ns have the best results; for thickness error (Z), choosing phase velocity at 0.2 m/ns is better; when frequency is 250 MHz, for permittivity error (K), choosing 0.2 m/ns is better; and for thickness error (Z), choosing max phase velocity is better (Figure 4.1 and Figure 4.2).

For Experiment 3, starting phase velocity at max (average 0.35 m/ns), that are only five points of 1000 MHz and 500 MHz, but there are enough points of 250 MHz to analyze its pattern. For 1000 MHz, permittivity and thickness error starting phase velocity at max is not as good as starting phase velocity at 0.2 m/ns, the error of inversion is also greater than starting phase velocity at 0.2 m/ns, and it increases with soil thickness. For 500 MHz, permittivity and thickness error starting phase velocity at max is very similar with starting at 0.2 m/ns, but max phase velocity has a better result and the error of inversion decreases with soil thickness. For 250 MHz, permittivity and thickness error, choosing max phase velocity is not as good as choosing 0.2 m/ns, and the error of inversion increase with soil thickness.

For starting phase velocity at 0.2 m/ns, 1000 MHz only has four points. Its permittivity and thickness error are both better than starting phase velocity at max, and the error of inversion decreases with soil thickness. For 500 MHz, permittivity and thickness error, starting phase velocity at 0.2 m/ns is very similar to starting at max, and the error of inversion increases with soil thickness. For 250 MHz, permittivity and

thickness error choosing phase velocity at 0.2 m/ns is better than choosing at max, and the error of inversion increases with soil thickness.

For starting phase velocity at 0.15 m/ns, 1000 MHz has no points, 500 MHz only has one point, and 250 MHz only have two points, so they all have too few data points for detailed analysis.

Experiment 4 was the foundation of dry organic loam covered by an incremental layer of saturated organic loam. For Experiment 4 data, choosing starting phase velocity at 0.15 m/ns has the same data number as choosing phase velocity at max and 0.2 m/ns, so only in this Experiment compared all three-different phase velocity. For all frequencies (1000 MHz, 500 MHz, and 250 MHz), starting at 0.15 m/ns gives the best result for the error of permittivity, thickness, and inversion (Figure 4.3, Figure 4.4, and Figure 4.5).

Figure 4.3. Experiment 4, 1000 MHz, permittivity and thickness error for three-phase velocities.

For starting phase velocity at 0.2 m/ns, 1000 MHz, permittivity and thickness error's results are similar with starting phase velocity at max and 0.15 m/ns, the error of inversion increases with soil thickness.

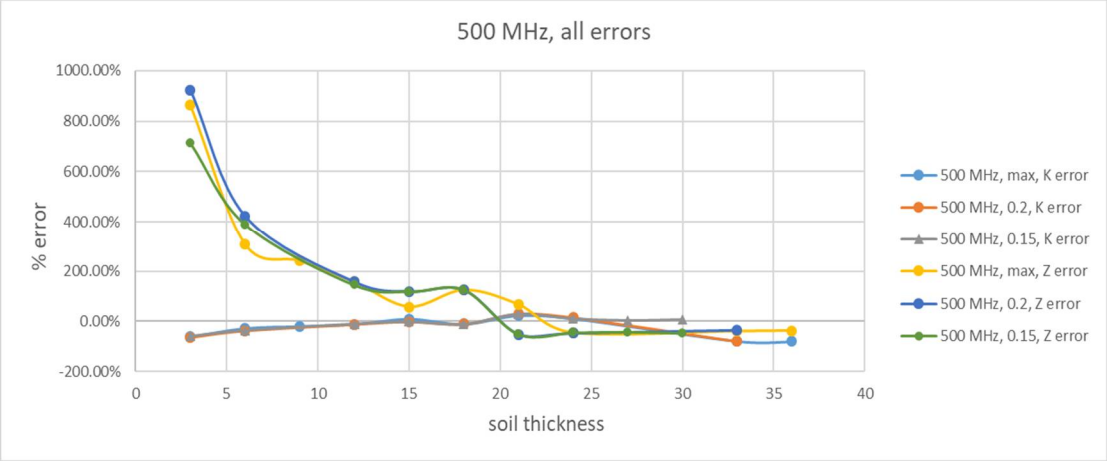

Figure 4.4. Experiment 4, 500 MHz, permittivity and thickness error for three-phase velocities.

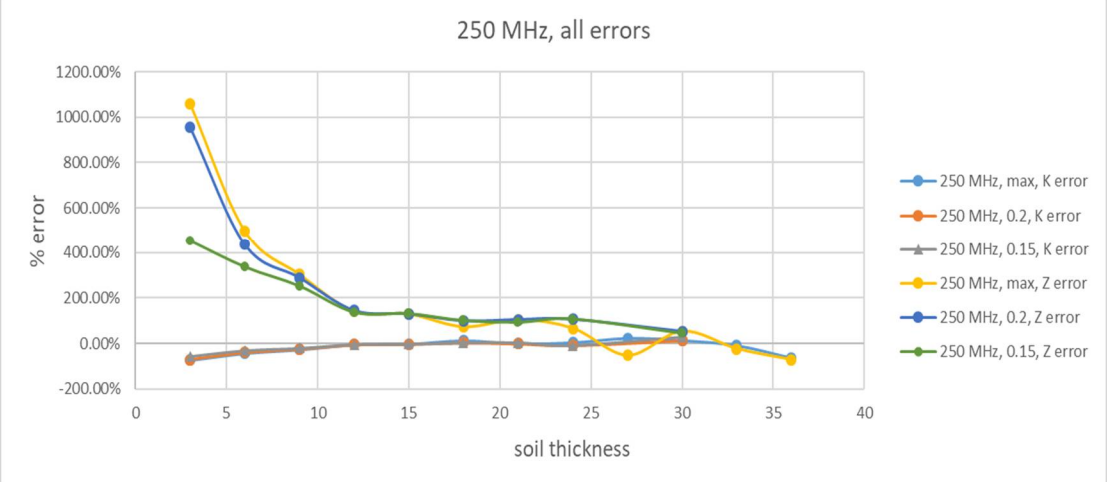

Figure 4.5. Experiment 4, 250 MHz, permittivity and thickness error for three-phase velocities.

For 500 MHz, permittivity and thickness error starting phase velocity at 0.2 m/ns is very similar with starting at max and 0.15 m/ns, the error of inversion decreases with soil thickness. For 250 MHz, permittivity and thickness error starting phase velocity at 0.2 m/ns is similar to starting at max and 0.15 m/ns, the error of inversion decreases with soil thickness.

For starting phase velocity at 0.15 m/ns, 1000 MHz, 500 MHz, and 250 MHz, permittivity and thickness error all have best results. For 1000 MHz, the error of inversion increases with soil thickness. For 500 MHz, the error of inversion decreases with soil thickness. For 250 MHz, the error of inversion increases with soil thickness. Experiment 5 was saturated with a silt base layer covered by a dry silt layer. for permittivity error (K) and thickness error (Z) of 1000 MHz and 250 MHz data of Experiment 5, choosing phase velocity at max have best results. For 500 MHz, thickness error (Z), choosing 0.2 m/ns is best, but for permittivity error (K), choosing max phase velocity is best. For the error of inversion, choosing 0.2 m/ns is better than choosing max phase velocity.

For Experiment 5 starting at max (average 0.3 m/ns), 1000 MHz, 500 MHz, and 250 MHz, max got best results for permittivity error and thickness error, but the error of inversion is not good enough. For 1000 MHz, the error of inversion decreases with soil thickness. For 500 MHz, the error of inversion decreases with soil thickness. For 250 MHz, the error of inversion increases with soil thickness (Figure 4.6 and Figure 4.7).

When starting phase velocity at 0.2 m/ns, 1000 MHz only has three points, and thus is was impossible to analyze its permittivity and thickness error pattern; there were five points for 500 MHz and 250 MHz. For permittivity error and thickness error

choosing phase velocity at 0.2 m/ns is not the best but for error of inversion, starting at 0.2 m/ns has a lower error than starting at max. For 1000 MHz, the error of inversion decreases with soil thickness. For 500 MHz, the error of inversion increases with soil thickness. For 250 MHz, the error decreases with soil thickness.

When starting phase velocity at 0.15 m/ns, Experiment 5 only has one point for 1000 MHz, and no point for 500 MHz and 250 MHz.

Experiment 6 had a dry silt base layer covered with an incremental layer of saturated silt. For permittivity error (K) and thickness error (Z) of 1000 MHz and 500 MHz data of Experiment 6, choosing max phase velocity give the best result; 250 MHz, for permittivity error (K), choosing max phase velocity is best, but for thickness error (Z), choosing phase velocity at 0.2 m/ns is best. But for error of inversion, choosing phase velocity at 0.2 m/ns is better than choosing max (Figure 4.8 and Figure 4.9).

For starting phase velocity at max (average 0.27 m/ns for Experiment 6), 1000 MHz only have three points; for 500 MHz, Experiment 6 has similar result as Experiment 5, choosing max phase velocity give best results for permittivity error and thickness error, but error of inversion is not good enough, it increases with soil thickness; and 250 MHz, for permittivity error (K), choosing max phase velocity is best, but for thickness error (Z), choosing 0.2 m/ns is best, the error of inversion decreases with soil thickness.

When starting phase velocity at 0.2 m/ns, 1000 MHz, no point can be chosen. For permittivity error of 500 MHz, starting phase velocity at 0.2 m/ns is similar to starting at max. For thickness error of 500 MHz, starting phase velocity at 0.2 m/ns is not as good as starting at max. The error of inversion of 500 MHz decreases with soil thickness. For permittivity error (K) of 250 MHz, choosing max phase velocity has the best result, for

thickness error (Z), choosing 0.2 m/ns is better. The error of inversion decreases with soil thickness.

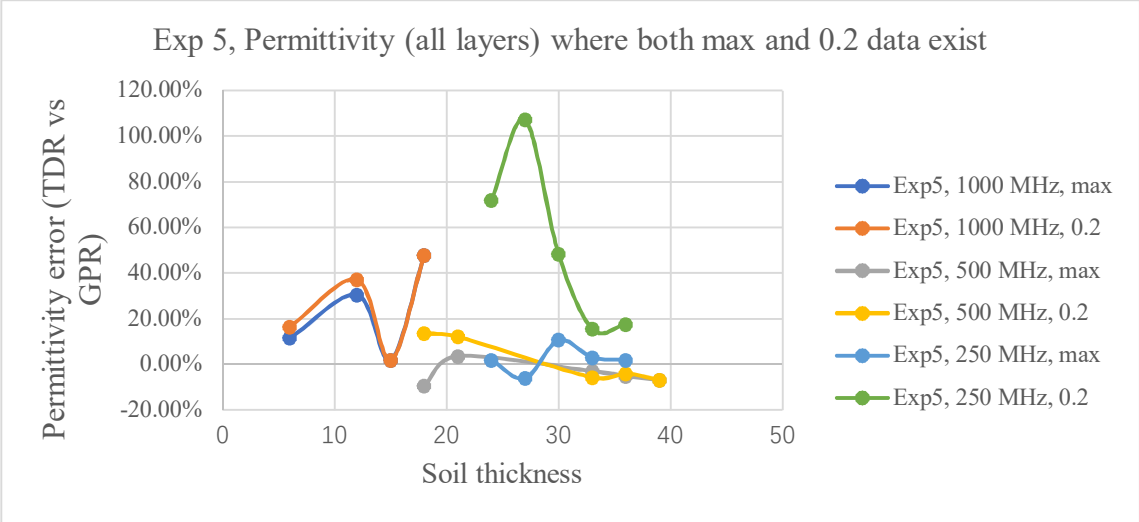

Figure 4.6. Experiment 5, permittivity (all layers) where both max and 0.2 m/ns data exist.

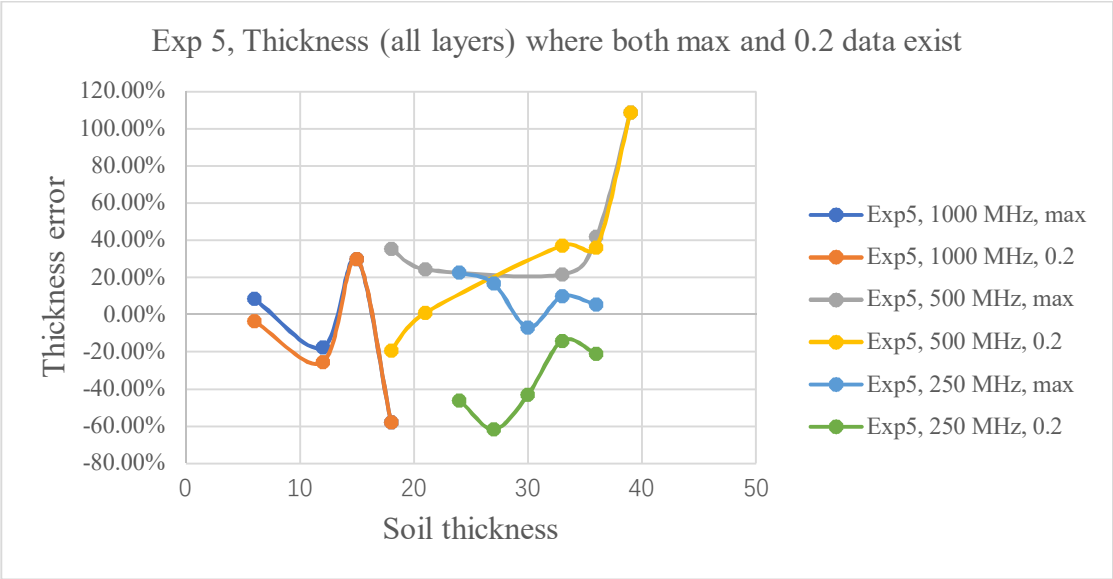

Figure 4.7. Experiment 5, thickness (all layers) where both max and 0.2 m/ns data exist.

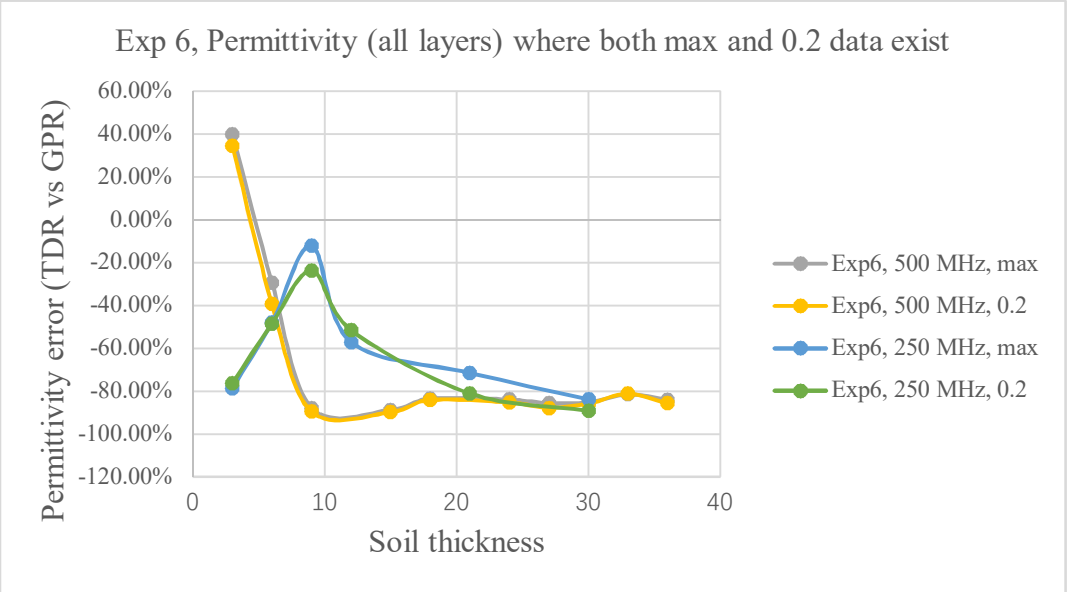

Figure 4.8. Experiment 6, permittivity (all layers) where both max and 0.2 m/ns data exist.

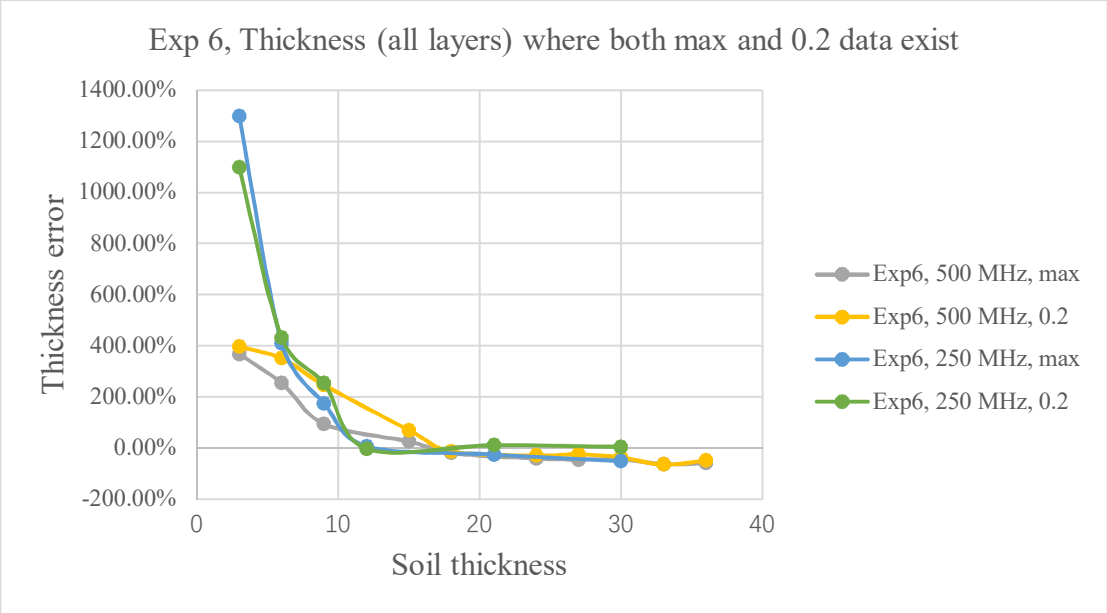

Figure 4.9. Experiment 6, thickness (all layers) where both max and 0.2 m/ns data exist.

When starting phase velocity at 0.15 m/ns, Experiment 6 does not have a point for 1000 MHz but have two points for 500 MHz and four points for 250 MHz. For Experiment 6, 250 MHz, the error of inversion increases with soil thickness.

For Experiment 3, 5, and 6, about the same permittivity and thickness estimates are obtained if we pick the starting phase velocity at max or 0.2 m/ns. But, for all Experiments, the inversion error was least when the starting phase velocity was at 0.2 m/ns. For these Experiments, the phase velocity often did not fall below 0.15 m/ns, so the results here apply only to higher starting phase velocities. For some frequencies, better estimates of permittivity were obtained with max, while better thickness estimates were obtained with 0.2 m/ns, but this wasn't a consistent pattern. Sometimes better estimates of permittivity were obtained with 0.2 m/ns, while better estimates of thickness were obtained with max.

Experiment 4 is quite different. For all frequencies, starting at 0.15 m/ns gives the best result for the error of permittivity, thickness, and inversion. Experiment 4 was wet organic soil overlying by dry organic soil. The soil was still mostly sand but had 10% organic fines, which made it act like an organic soil. For this soil, lower starting velocities were better.

There does not appeared to have a relationship between water content and processing parameters, as wet and dry soil showed similar results for different starting phase velocities. Experiments 3 and 5 both had dry soil overlying by wet soil, while Experiments 4 and 6 both had wet soil overlying by dry soil. For Experiment 3, no clear pattern was detected for best estimates of permittivity and thickness as a function of starting velocity. For Experiment 5, the maximum starting velocity was usually the best.

For Experiment 4 (wet soil overlying dry), the lowest starting velocity provided the most accurate results, while for Experiment 6 (also wet soil overlying dry), the max starting velocity was usually the best. Since no consistent pattern could be observed in dry versus wet soil, it does not appear that unclear water content affects the best starting velocities.

Processing parameters may be influenced by soil texture. In most cases, for organic loam layers (Experiment 3 and 4), the lower the starting phase velocity, the accurate the results; for silt layers (Experiment 5 and 6), the pattern is the opposite, the higher the starting point, the accurate the results. The organic loam is 92% sand with 8% organic material, and silt is more than 90% fine-grained material. For the organic loam, there is less attenuation and can see better results when focus on the lower end of the dispersion curve (lower phase velocities and higher frequencies). For the silt, there is more attenuation to occur, because it has much more fine-grained material than the organic loam. The silt can see better results when focus on the entire dispersion curve (higher phase velocities and lower frequencies). In this research, only studied the fundamental mode, so high-frequency energy is associated with lower phase velocities. Higher frequency energy attenuates more rapidly than lower frequency energy. It is possible that attenuation of high frequencies makes the lower end of the dispersion curve less accurate for soils with lots of attenuation (like silt). For soils with less attenuation (like organic loam/sand), focusing on the lower end of the dispersion curve, where the error of inversion is less, gave better results. To confirm this hypothesis more research with different soil textures would be needed.

Therefore, for the fundamental mode, choosing the maximum starting phase velocity is usually best or equivalent to choosing a lower starting phase velocity. For

some wet soils that have low attenuation, it may be better to choose a lower starting phase velocity. The error of inversion is less for lower starting phase velocities, so this should be considered when evaluating the accuracy of inversion estimates.

REFERENCES

Arcone, S.A., Peapples, P.R., Liu, L., 2003. Propagation of a ground-penetrating radar (GPR) pulse in a thin-surface waveguide. Geophysics, 68(6): 1922-1933.

Bikowski, J., Huisman, J.A., Vrugt, J.A., Vereecken, H., van Der Kruk, J., 2012. Integrated analysis of waveguide dispersed GPR pulses using deterministic and Bayesian inversion methods. Near Surface Geophysics, 10(6): 641- 652. DOI:10.3997/1873-0604.2012041.

Busch, S., Van Der Kruk, J., Bikowski, J., Vereecken, H., 2012. Quantitative conductivity and permittivity estimation using full-waveform inversion of on-ground GPR data. Geophysics, 77(6): H79-H91. DOI:10.1190/geo2012-0045.1.

Galagedara, L.W., Parkin, G.W., Redman, J.D., von Bertoldi, P., Endres, A.L., 2005.Field studies of the GPR ground wave method for estimating soil water content during irrigation and drainage. Journal of Hydrology, 301(1–4): 182-197. DOI:http://dx.doi.org/10.1016/j.jhydrol.2004.06.031.

Hajiani, Payman., 2016. Identifying shallow subsurface stratigraphy and voids using dispersive characteristics of electromagnetic and surface waves. Doctoral Dissertations. 2578.

Liu, L., Arcone, S., 2003. Numerical Simulation of the Wave-Guide Effect of the Near-Surface Thin Layer on Radar Wave Propagation. Journal of Environmental and Engineering Geophysics, 8(2): 133-141. DOI:10.4133/JEEG8.2.133.

Mangel, A.R., Lytle, B.A., Moysey, S.M.J., 2015a. Automated high-resolution GPR data collection for monitoring dynamic hydrologic processes in two and three dimensions. Leading Edge, 34(2): 190-196. DOI:10.1190/tle34020190.1.

Mangel, A.R., Moysey, S.M.J., van der Kruk, J., 2015b. Resolving precipitation induced water content profiles by inversion of dispersive GPR data: A numerical study. Journal of Hydrology, 525: 496-505 DOI:http://dx.doi.org/10.1016/j.jhydrol.2015.04.011.

Park, C.B., Miller, R.D., Xia, J., 1998. Imaging dispersion curves of surface waves on multi-channel record, 68th Ann. Internat. Mtg., Soc. Expl. Geophys., pp. 1377-1380.

Park, C.B., Miller, R.D., Xia, J., 1999. Multichannel analysis of surface waves. Geophysics, 64(3): 800-808.

Rege, R. and Godio, A., 2009. Inversion of guided waves in georadar data. 2009 IEEE.

Van Der Kruk, J., 2006. Properties of surface waveguides derived from inversion of fundamental and higher mode dispersive GPR data. IEEE Transactions on Geoscience and Remote Sensing, 44(10): 2908-2915. DOI:10.1109/TGRS.2006.877286.

Van der Kruk, J., Streich, R., Green, A.G., 2006. Properties of surface waveguides derived from separate and joint inversion of dispersive TE and TM GPR data. Geophysics, 71(1): K19-K29. DOI:10.1190/1.2168011.

Van Der Kruk, J., Arcone, S.A., Liu, L., 2007. Fundamental and higher mode inversion of dispersed GPR waves propagating in an ice layer. IEEE Transactions on Geoscience and Remote Sensing, 45(8): 2483-2491 DOI:10.1109/TGRS.2007.900685.

Van der Kruk, J., Jacob, R.W., Vereecken, H., 2010. Properties of precipitation-induced multilayer surface waveguides derived from inversion of dispersive TE and TM GPR data. Geophysics, 75(4): XWA263-WA273 DOI:10.1190/1.3467444.

Van Der Kruk, J., Steelman, C.M., Endres, A.L., Vereecken, H., 2009a. Dispersion inversion of electromagnetic pulse propagation within freezing and thawing soil waveguides. Geophysical Research Letters, 36(18) DOI:10.1029/2009GL039581.

Van der Kruk, J., Vereecken, H., Jcob, R.W., 2009b. Identifying dispersive GPR signals and inverting for surface wave-guide properties. Leading Edge (Tulsa, OK), 28(10): 1234-1239. DOI:10.1190/1.3249780.

Xiao, X., Ihamouten, A., Villain, G. and Dérobert, X., 2016. Use of E lectromagneticTwo-layer Wave-Guided Propagation in the GPR Frequency Range to Characterize Water Transfer in Concrete DOI: 10.1016/j.ndteint.2016.08.001.

VITA

Yunyi Guan was born in Daqing City, China. In 2015 graduated from Northeast Petroleum University, China, and received Bachelor of Engineering degree in Resources Exploration Engineering.

She obtained field geology practical experience during the summer internship in Qinhuangdao, China in 2012 and 2013. In 2014, she learned about the basic knowledge of the pumping unit and oil production process during the internship in the Fourth Oil Extraction Plant of Daqing Oilfield Company.

In 2015, Ms. Guan participated in the Oil and Gas Engineering Institute of PetroChina Jilin Oilfield Company as an employee and worked on the project research of oil production test engineering.

In August 2017, she received admission to study geological engineering (M.S) at Missouri University of Science and Technology in Rolla, Missouri, US. She received her Master of Science in Geological Engineering from Missouri University of Science and Technology in December 2018